

TA7
W34c
no. SL-94-1
c.2

Contract Report SL-94-1
February 1994

**US Army Corps
of Engineers**
Waterways Experiment
Station

Constitutive Modeling of Rocks with Internal Cracks and Pores

*by D. Krajcinovic, V. Lubarda
Arizona State University*

WES

Approved For Public Release; Distribution Is Unlimited

Contract Report SL-94-1
February 1994

Constitutive Modeling of Rocks with Internal Cracks and Pores

by D. Krajcinovic, V. Lubarda

Arizona State University
Department of Mechanical
and Aerospace Engineering
Tempe, AZ 85287-6106

Final report

Approved for public release; distribution is unlimited

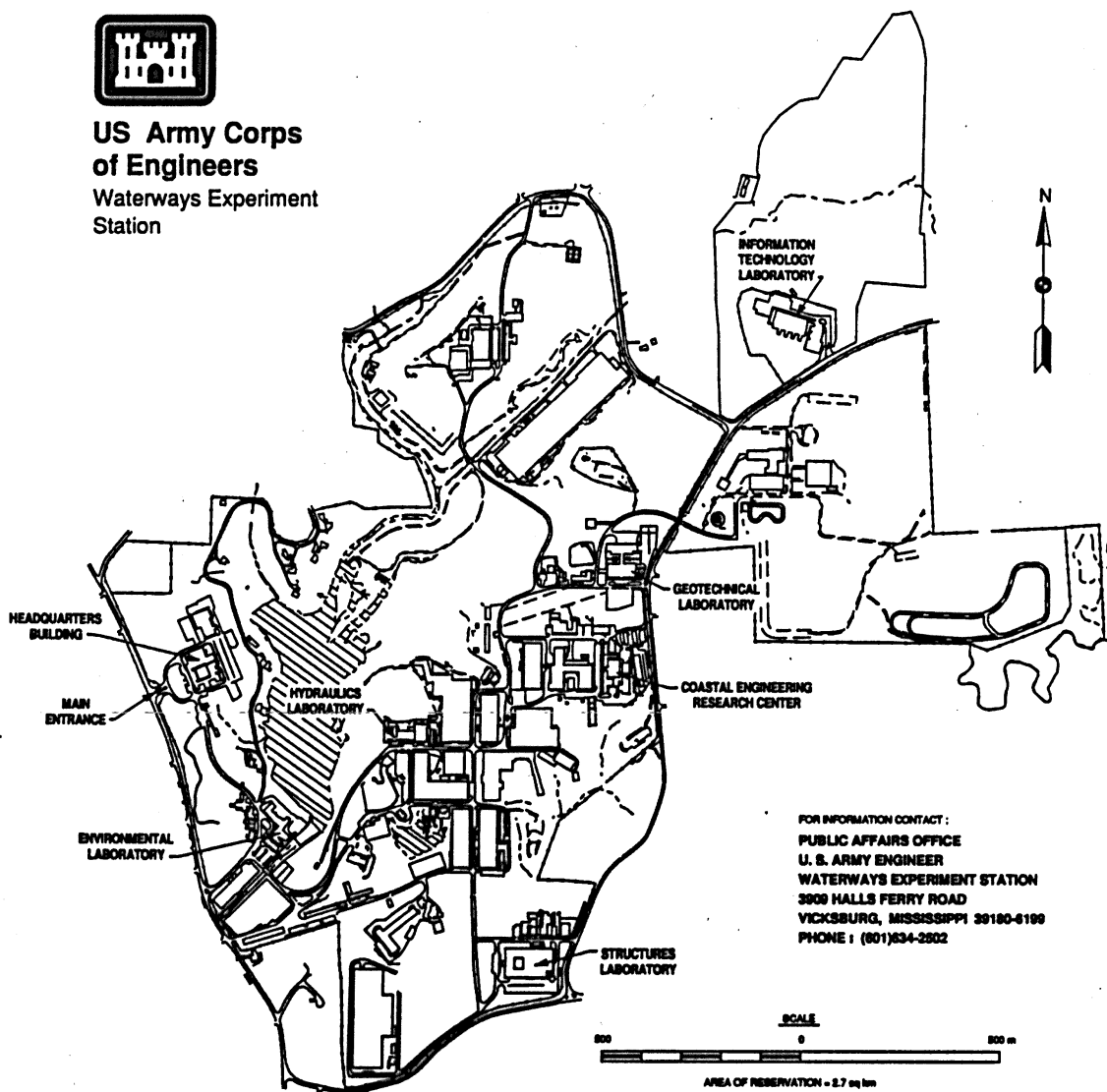
Prepared for Defense Nuclear Agency (SPWE)
6801 Telegraph Road
Alexandria, VA 22310-3398

Under FY92 Work Unit Code 00002 (Task 4)

Monitored by Structures Laboratory
U.S. Army Engineer Waterways Experiment Station
3909 Halls Ferry Road, Vicksburg, MS 39180-6199



**US Army Corps
of Engineers**
Waterways Experiment
Station



Waterways Experiment Station Cataloging-In-Publication Data

Krajcinovic, Dusan

Constitutive modeling of rocks with internal cracks and pores / by D. Krajcinovic, V. Lubarda ; prepared for Defense Nuclear Agency ; monitored by Structures Laboratory , U.S. Army Engineer Waterways Experiment Station.

70 p. : 28 cm. — (Contract report ; SL-94-1)

Includes bibliographical references.

1. Rock mechanics — Mathematical models. 2. Deformation (Mechanics) 3. Micromechanics. I. Lubarda, Vojislav II. United States. Defense Nuclear Agency. III. U.S. Army Engineer Waterways Experiment Station. IV. Title. V. Series: Contract report (U.S. Army Engineer Waterways Experiment Station) ; SL-94-1.

TA7 W34c no.SL-94-1

PREFACE

The investigation reported herein was conducted at Arizona State University (ASU) under Contract No. DACA39-92-M-1980 for the U.S. Army Engineer Waterways Experiment Station (WES). The research was performed during the period March 1992 to October 1992. Funding was provided by the Defense Nuclear Agency (DNA), Shock Physics Directorate, Weapons Effects Division (SPWE). The DNA Project Monitor was Dr. Edward L. Tremba, SPWE.

The principal investigator at ASU was Professor Dusan Krajcinovic. He was assisted in this work by Dr. Vlado Lubarda, a Visiting Associate Professor at ASU.

The work was technically supported and monitored by WES Contracting Officer's Representative, Dr. Behzad Rohani, Geomechanics Division (GD), Structures Laboratory (SL), and his colleague, Dr. Joseph S. Zelasko, GD. Dr. J.G. Jackson, Jr., was Chief, GD, at the time this work was performed. Mr. Bryant Mather was Director, SL.

At the time of publication of this report, Director of WES was Dr. Robert W. Whalin. Commander was Col Bruce K. Howard, EN.

This page intentionally left blank

TABLE OF CONTENTS

| <i>Section</i> | <i>Page</i> |
|--|-------------|
| PREFACE | i |
| LIST OF FIGURES | v |
| CONVERSION FACTORS FOR U.S. CUSTOMARY TO SI UNITS OF MEASUREMENT | vii |
| 1.0 INTRODUCTION | 1 |
| 2.0 MICROMECHANICS OF BRITTLE DEFORMATION PROCESSES IN POROUS ROCKS | 4 |
| 2.1. Experimental Observations | 5 |
| 2.2. Cylindrical Pore Model | 8 |
| 2.3. Brittle-Ductile Transition | 11 |
| 3.0 PHENOMENOLOGICAL DAMAGE MODELS FOR BRITTLE DEFORMATION OF ROCKS | 15 |
| 3.1. Crack Density Distribution | 15 |
| 3.1.1. Second- and Fourth-Order Approximations | 18 |
| 3.1.2. Negative Crack Density—Anticracks | 20 |
| 3.1.3. Rose Diagram | 23 |
| 3.2. Representation of Damage | 24 |
| 3.3. Elastic Stiffness Tensor | 25 |
| 3.3.1. Isotropic Damage | 27 |
| 3.3.2. Transversely Isotropic Damage | 28 |
| 3.4. Elastic Compliance Tensor | 29 |
| 3.5. Applications | 31 |
| 3.5.1. Uniaxial Loading | 31 |
| 3.5.2. Biaxial Loading | 34 |

| | |
|--|----|
| 4.0 MICROMECHANICALLY INSPIRED DAMAGE MODELS FOR BRITTLE DEFORMATION OF ROCKS | 35 |
| 4.1. Elastic Body Containing a Penny-Shaped Crack | 35 |
| 4.2. Averaging Procedure | 39 |
| 4.3. Effective Compliance Tensor | 42 |
| 4.4. Effective Stiffness Tensor | 44 |
| 4.5. Axial Compression of a Laterally Confined Specimen | 46 |
| 5.0 SUMMARY AND CONCLUSIONS | 49 |
| 6.0 REFERENCES | 51 |

LIST OF FIGURES

| Figure | Page |
|--|------|
| 2.1. Cylindrical pore of radius R under remote compressive stress σ^0 | 8 |
| 2.2. Two interacting cylindrical pores under remote compressive stress σ^0 | 9 |
| 2.3. A notched void of radius R and crack length a | 10 |
| 2.4. Normalized stress-intensity factor vs. aspect ratio a/R , for several different confinement ratios φ | 11 |
| 2.5. Normalized stress-intensity factor vs. aspect ratio a/R , for several different values of porosity f and two confinement ratios φ | 13 |
| 3.1. (a) Crack distribution within orthogonal crack families modeled by a continuous crack distribution of oval shape; (b) If the crack densities are the same, the oval shape becomes spherical, giving rise to an isotropic damage distribution; (c) Crack distribution corresponding to inclined crack families | 16 |
| 3.2. Second- and fourth-order continuous approximations of two orthogonal crack families with the same crack densities | 19 |
| 3.3. Second- and fourth-order continuous approximations of a single crack family . . . | 21 |
| 3.4. Continuous crack distributions corresponding to two orthogonal crack families of different crack density ratios | 22 |
| 3.5. (a) A "rose diagram" deduced from actual test measurements. The representative crack densities are: $\rho_1 = \rho_5 = 1.8\rho_0/2\pi$, $\rho_2 = 14.4\rho_0/2\pi$, $\rho_3 = 10.8\rho_0/2\pi$, and $\rho_4 = 7.2\rho_0/2\pi$, where ρ_0 is the total crack density; (b) Continuous second-order approximation for crack density distribution corresponding to the above "rose diagram". | 23 |

LIST OF FIGURES (Concluded)

| Figure | Page |
|--|------|
| <p>3.6. (a) Planar distribution of cracks: all cracks have their normals parallel to the longitudinal direction; (b) Cylindrical distribution of cracks: all cracks have their normals orthogonal to the longitudinal direction</p> | 31 |
| <p>3.7. (a) Volumetric stress-strain response corresponding to eqn (3.41) of text: σ is the compressive stress, and E_{kk} is the corresponding volumetric strain, κ_0 is the undamaged bulk modulus; (b) Stress-strain response corresponding to eqn (3.49) of text: σ is the magnitude of the biaxial tension, and ϵ is the corresponding strain, E_0 and ν_0 are the undamaged Young's modulus and Poisson's ratio</p> | 33 |
| <p>4.1. Penny-shaped crack of radius a and circumference l: $(1', 2', 3')$ denotes local crack coordinate system, direction $1'$ being coincident with normal to crack plane m; angles θ and ϕ define orientation of vector m relative to global coordinate system $(1, 2, 3)$</p> | 36 |
| <p>4.2. Local tensile stress σ^* (which drives the microcrack growth) arises in the vicinity of the pore</p> | 48 |

**CONVERSION FACTORS FOR U.S. CUSTOMARY TO SI
UNITS OF MEASUREMENT**

Non-SI units of measurement used in this report can be converted to SI units as follows:

| | | |
|------------------------|------------------|-------------------------|
| <u><i>Multiply</i></u> | <u><i>By</i></u> | <u><i>To Obtain</i></u> |
| degree (angle) | 0.01745329 | radian |

This page intentionally left blank

CONSTITUTIVE MODELING OF ROCKS WITH INTERNAL CRACKS AND PORES

1.0 INTRODUCTION

The brittle deformation processes in materials such as rocks, concretes, ceramics, etc., have lately attracted a great deal of attention. On the microscale this class of deformation processes is characterized by the cooperative evolution of a large number of crack-like microdefects of irregular geometry. The complexity of the problem is further exacerbated by the dependence of the crack growth and the stiffness on the sign of normal stresses. Early constitutive models were based on modifications of the venerable plasticity theory originally intended to predict the behavior of ductile metals. The inability of these models to predict the brittle response of rocks stimulated efforts to examine the underlying micromechanical processes. Constitutive analysis which captures salient aspects of the micromechanical processes characteristic of particular materials and applications, which is still reasonably simple, is, therefore, highly desirable.

The early micromechanical models addressed primarily the dependence of elastic moduli on the microdefect density. Budiansky and O'Connell (1976) considered randomly distributed flat cracks and applied the self-consistent method to obtain the effective elastic properties of the overall isotropic response. In this analysis all cracks were supposed to be open during loading. In the case when some cracks close or undergo frictional sliding, the overall response becomes anisotropic and load-path dependent (Hori and Nemat-Nasser, 1983). Sammis and Ashby (1986) developed an approximate theory to predict the failure of brittle porous solids, loaded in compression, during which cracks grow from the surfaces of the preexisting pores or vacancies. Nemat-Nasser and Obata (1988), in their micromechanical modeling of the inelastic response of brittle materials such as compact rocks, concrete and some ceramics, used the sliding crack mechanism as the dominant source of inelasticity. According to this model the frictional sliding of preexisting cracks leads to the formation of tension wing-cracks (see also Kachanov, 1982, and Ashby and Hallam, 1986). A dilute distribution of preexisting cracks was assumed, neglecting interaction among neighboring flaws.

Other mechanisms of microcracking in rocks, such as elastic mismatch and bending mechanisms, were also suggested. For heterogeneous materials, the local tensile stresses appear at the interface of two elastically mismatched materials. Tensile stresses resulting from the unequal lateral expansion of the mismatched materials are often sufficient to cause nucleation and subsequent

propagation of a microcrack (Kemeny and Cook, 1991). According to the bending model, the tensile stress needed to trigger microcrack growth occurs as a result of bending a soft and elongated particle spanning two harder inclusions. Extensive summaries and reviews on microcracks in rocks are given by Kranz (1983), Zheng (1989), and others.

The behavior of brittle rocks with inferior tensile strength depends on the mode and stability of the crack growth. Thus, the response of a brittle rock subjected to compressive loading strongly depends on the lateral confinement. An unconfined specimen containing a large number of flaws fails by axial splitting or slabbing (Horii and Nemat-Nasser, 1986). Final failure occurs as a result of the unstable growth of a single crack of preferential geometry at a relatively small microcrack density. Thus, the microcrack interaction is relegated to a second-order effect. As the confinement is increased, axial splitting is suppressed and a typical rock specimen fails by formation of a narrow region of high crack density (fault or "shear band"). Finally, at large levels of lateral confinement, homogeneous microcracking prevails throughout the sample, resulting in a quasi-ductile overall response. The microcrack density (especially within the "shear band" emerging near the apex of the force-displacement curve) is in this case much more substantial, rendering microcrack interaction not only important but even the dominant factor of failure. The degree of confinement at which the mode of failure changes is referred to in rock mechanics as the brittle-to-ductile transition. This phenomenon was studied by many authors, most recently by Hirth and Tullis (1989), Wong (1990), and Zhang, *et al.* (1990a,b).

The micromechanical studies reported in the literature have demonstrated all of the advantages and disadvantages of micromechanical models. The relative absence of ambiguity, direct identification of material parameters, and conceptual clarity of micromechanical models are accompanied by a lack of computational efficiency and limitations to simple geometries and homogeneous states of stress. By its very nature the micromechanical determination of the state of damage at a material point of an effective continuum involves compilation of records defining the growth of each microcrack within the corresponding representative volume element of the actual material. The attendant bookkeeping and averaging represents a formidable problem which may be redundant since it is not immediately known how detailed the information sought must be. Thus, as stated by Rice (1975), a direct micromechanical prediction of material response is unlikely to displace the application of phenomenological and less rigorously based structure-parameter models.

Unfortunately, the state of the art of phenomenological modeling is far from satisfactory. In the wake of the original Kachanov model (1958), in which damage was measured by a scalar, different and contradictory choices of other damage variables were promoted as proper characterizations of the deterioration of the material properties. Vectorial, second-order, and fourth-order tensor representations of damage were proposed to capture the damage-induced anisotropy (Vakulenko and Kachanov, 1971, Dragon and Mroz, 1979, Kachanov, 1980, Krajcinovic and Fonseka, 1981,

Talreja, 1985, Costin, 1985, Murakami, 1988, Ju, 1989, Kachanov, 1992, etc.). The phenomenological features of damage mechanics theory, such as damage surface and damage rule, analogous to yield surface and flow rule of the more developed phenomenological metal plasticity theory, are still in the early stages of development and are the subject of ongoing active research (Simo and Ju, 1987, Chow and Wang, 1988, Krajcinovic, 1989, Chaboche, 1992, etc.). Moreover, the relation of these models to the physics of the phenomenon is often less than obvious.

A third class of models makes an attempt to combine the desirable attributes of micromechanical and phenomenological theories. Rudnicki and Rice (1975) treat the onset of rupture in brittle rock masses as a constitutive instability. Their macroscopic constitutive equations are the pressure-dependent generalization of the Prandtl-Reuss equations of metal plasticity. Inelastic response, dilatant in nature, was considered to be predominately a consequence of the frictional sliding on microcrack surfaces, their uplifting over asperities, and tensile cracking into the crack wings (kinks). Nemat-Nasser and Shokoh (1980) further developed these constitutive equations to account for inelastic volume changes and pressure sensitivity, important in geotechnical materials such as cohesionless sands and cohesive soils. Ortiz (1985) considered a constitutive model for the inelastic behavior of concrete, by viewing it as a mixture of two phases: mortar and aggregate. Simple models were used to describe the individual responses of mortar and aggregate, and mixture theory was implemented to obtain the overall composite response. None of the existing models, however, satisfies the contradicting requirements of rigor and simplicity. Moreover, none of these models was used successfully, if at all, for large-scale computations or for a general case of loading.

The objective of the present study is neither to recapitulate the current state of micromechanical and phenomenological modeling nor to reconcile all or even most existing theories singling out those that do not satisfy all conditions. Instead, the ultimate objective is to formulate a microscopically-inspired continuum model which will be suitable for large-scale computations. While retaining as much generality as possible, the proposed model will specifically address the brittle deformation processes in porous sandstone and limestone rocks. Ductile deformation will be considered in a following study. In view of the many competing models, it seems reasonable to revisit the problem from its very start and examine the approximations related to the representation of the existing distribution of microcracks by an appropriate tensor measure. Additionally, the present study will reexamine the mathematical structure of the effective compliances and stiffnesses demonstrating that rigor can be preserved without attendant sacrifices in simplicity. At this point a second-order tensor representation of damage will be considered and the damage-induced anisotropy will be approximated by orthotropy. A more complete discussion of the problem, within the framework formulated herein, including considerations of other types of anisotropy and extensions to rate theories, will be presented subsequently.

2.0 MICROMECHANICS OF BRITTLE DEFORMATION PROCESSES IN POROUS ROCKS

The word rock refers to a large class of naturally formed solid materials of different structure and chemical composition. Near the exposed surface, most rocks are weathered and fragmented. The stresses to which the rocks are exposed in engineering application are often inferior to stresses developed during their formation or tectonic movements. As a result, a typical rock contains crack-like defects on a range of scales. From the geological and seismic viewpoint the most important defects are joints and faults with lengths measured in tens and hundreds of miles. Our current interest, however, is centered on studying the influence of relatively small defects on the mechanical response of rock specimens which do not contain joints, tested in the laboratory.

The mechanical response and strength of a rock is to a large degree determined by its microstructure (or fabric). The fabric of a typical rock encompasses crystal aggregates joined together by some cementitious material. Preferred crystal orientations, bedding planes, foliation, schistosity, microfissures, and porosity, common to rocks, are the principal reasons for preferred directions, anisotropy, and reduction of the mechanical strength (see, for example, Jaeger and Cook, 1976).

As a consequence of their inferior tensile strength rocks are subjected primarily to compressive loadings in engineering applications. The average (macro) normal stresses are seldom if ever tensile. However, the local stress fluctuations, attributable to the inhomogeneities in the rock fabric, will, in general, have tensile components as well. These local tensile stresses are in most cases considered to be the principal reason for microcracking. The distribution and magnitude of these local stresses depends on the shape of the inhomogeneity, elastic mismatch, defect density, etc. Thus, the determination of the local stress from the average stress requires a micromechanical study based on the actual rock fabric.

Some of the definitions used in rock mechanics are a direct consequence of the idiosyncrasies of the deformation process in rocks. The conventional crystal plasticity mechanisms are operative in low-porosity crystalline rocks only at high temperatures (Evans, *et al.*, 1990). In all other cases the inelastic deformation is attributed to the nucleation, propagation, and coalescence of microcracks into larger clusters. For example, in porous rocks macroscopic ductility reflects distributed grain-scale crushing and microcracking (Wong, 1990). The mode and stability of microcracking depends on the ratio of the hydrostatic pressure and deviatoric stress. Thus, the ductile deformation of porous rocks is dependent on the first invariant of the macrostress tensor (see Byerlee and Brace, 1969, Jones, 1980, etc.). The ductility of the deformation process is customarily defined by the character of the functional dependence of the axial strain on the hydrostatic and deviatoric stresses.

In stress-controlled tests at low confinement the mode of failure is brittle. The onset of failure is sudden and is not preceded by significant inelastic strains. In contrast, the much more

important behavior of rock specimens in confined conditions is rich in details and possibilities. In crustal conditions the deformation of rocks in the majority of cases is controlled by displacement constraints (confinement).

Deformation is referred to as being ductile on the macroscale when the increase of the axial strain in a specimen subjected to constant hydrostatic stress requires increase of the deviatoric stress. On the microlevel this typically means that the microcrack growth is stable, i.e., that the crack can grow only if the deviatoric stress is increased. In contrast, if in a displacement-controlled test the deviatoric stress reaches a maximum and starts declining at increasing axial strain the response is referred to as being brittle. The corresponding segment of the force-displacement curve is labeled as "softening". The softening phenomenon is readily explained on the microscale by the unstable growth of microcrack lengths. Depending on the ratio of the differential stress to the effective mean stress the ultimate failure at low temperatures can occur as a result of the localization of microcracks into a "crack (or shear) band" or by cataclastic flow (Paterson, 1978, Horii and Nemat-Nasser, 1986). The transition between the failure emphasizing inhomogeneous deformation (localization) and the failure characterized by homogeneous deformation (cataclastic flow) is referred to as the brittle-to-ductile transition (Rutter and Hadizadeh, 1991, Wong, *et al.*, 1992, etc.). At high confinement levels the deformation is homogeneous and the ultimate (or macro) failure takes place when the density of microdefects reaches critical concentration.

2.1. EXPERIMENTAL OBSERVATIONS

Even though the relation between the mode of deformation and microcrack evolution has been accepted as the dominant aspect of the phenomenon, the experimental data available in the literature are primarily related to macroscopic observation (Hustrulid and Robinson, 1973, Paterson, 1978, Felice, *et al.*, 1991). The present discussion (based on the literature) is confined to the low-temperature compression of sandstone rock specimens below the brittle-ductile transition. In a series of publications, Zhang, *et al.* (1989, 1990a,b), and Wong (1990) summarized an ambitious experimental program considering several different sandstone rocks using both nondestructive testing methods (Acoustic Emissions - AE) and Scanning Electron Microscope (SEM) micrographs. A substantial AE activity was characteristic of all samples tested regardless of the character of their macroscopic brittleness or ductility (Wong, 1990). Thus, by inference, a specimen is macroscopically brittle if the lateral confinement is insufficient to keep the microcrack growth stable. Conversely, if the microcrack growth is stable a specimen is macroscopically "ductile".

The series of papers listed in the above paragraph identified two major mechanisms of microcrack nucleation and growth. Hertzian contact stresses between calcite cement and quartz grains (elastic mismatch) were identified as the major micromechanical process leading to nucleation of cracks found in hydrostatically compressed sandstone samples. The contact stresses were determined by modeling the porous rock as a randomly packed assemblage of spherical particles.

Since the contact stress concentrations were highly localized, the initial microcrack length was found to be very short (ranging from 0.004 to 0.3 mm). The final crack lengths, radiating from the points of contact, seemed to be up to 1 mm long (see Fig. 6 in Zhang, *et al.*, 1990a). The second micromechanical mechanism of inelastic rock deformation was attributed to stress concentrations at the perimeter of voids. Sammis and Ashby (1986) have developed an analytical model for the latter mechanism based on fracture mechanics considerations, which sufficed for formulation of relations among the fracture toughness, the porosity, and the stress field (more specifically the ratio between the confining pressure and the maximum compressive stress).

Additional data regarding the SEM observations of microcrack density are available in Wong, *et al.* (1992). The crack densities in two orthogonal directions were determined using conventional stereological methods (Underwood, 1970, Wong and Biegel, 1985). In hydrostatically-loaded Berea sandstone specimens, the number of microcracks in two orthogonal planes was almost identical (with differences accounted for by bedding); however, a marked increase of microcracks parallel to the maximum compressive stress emerged when a differential stress was added to the already existing hydrostatic pressure. Thus, the deformation process, reflecting the sequence of different modes in which the microstructure changes, strongly depends on the manner in which the loads are applied. In other words, the deformation depends on whether the applied loading is proportional or not. In the language of applied mechanics, the deformation processes in the rock are strongly path dependent.

Precise data related to the angular distribution of cracks are even more difficult to find. Hallbauer, *et al.* (1973) carefully examined specimens of argillaceous quartzite and found that the majority of cracks were oriented within 10° to the compression axis*. Microcracks were rather short (0.1 to 1 mm in length), intragranular, and confined to single quartz grains. A similar conclusion was arrived at by Zheng, *et al.* (1991) who investigated compressive stress-induced microcracks in limestone. Most microcracks were formed by bending of long beam-like grains. In the case of large lateral confining stress (34 MPa) the microcracks were reasonably uniformly distributed over the entire volume of the specimen even in the post-peak regime. At a lateral confining stress of 17 MPa, localization into a few shear bands became apparent. At zero confining stress the damage in the post-peak regime was strongly localized into a single crack near the surface of the specimen parallel to the compressive axis. The rest of the specimen was in this case almost completely undamaged. According to the data in Zheng, *et al.* (1991) the average angle subtended by microcrack planes and the compressive axis did not exceed 15° . The microcrack density (defined as the number of cracks per unit area) was found to increase, and the microcrack length decrease, with an increase of confining stress. The crack-width to crack-length aspect ratio was typically 0.02. Somewhat older data for sandstone and limestone specimens are available in Swolfs (1972), Sangha, *et al.* (1974), Olsson (1974), and Conrad and Friedman (1976).

* See page vii for conversion to SI units.

Application of acoustic emissions to detect the location and intensity of microcracking in rocks has been suggested in the recent past by Holcomb and Costin (1986), Holcomb, *et al.* (1990), Lockner and Byerlee (1991), Lockner, *et al.* (1992), and others. According to these data (see Lockner, *et al.*, 1992) AE clustering was observed in Berea sandstone from the earliest stages of loading. Initially this clustering was found to be diffuse suggesting that the microcracks can grow only through interaction with adjacent defects. The level of localization was found to be directly proportional to the applied compressive force.

In summary, the available data set, while not complete, suffices to draw a number of important conclusions related to the inelastic deformation of sandstones. At low temperatures and stresses below the crushing level, the inelastic deformation of sandstone specimens is directly attributable to the nucleation, growth, and stability of microcracks. The specific mechanism of microcrack nucleation varies with microstructure. The growth of a single microcrack (which does not interact with other microdefects), generated from a pore, appears to be stable. Thus, the microcrack interaction problem appears to be instrumental in micromechanical modeling of microcrack growth. The distribution of microcrack sizes, shapes, and orientations depends on the microstructure (sizes of grains, pores, etc.) and the stress field. The brittle-ductile transition and the final failure mode depend on the level of confinement.

At this point it can be speculated that the available micromechanical data suffice to form the basis for an analytical model in the case of proportional loading, i.e., as long as the deformation process is dependent on a well documented sequence of dominating micromechanisms. More specifically, during proportional loading the active microcracks will likely remain active. Consequently, changes of the effective macroparameters (such as stiffness, elastic moduli, and accumulated damage) will change gradually and in orderly fashion. This type of problem is, for simplicity, best handled by deformation-type theories. In the case of non-proportional loadings characterized by rotation of the principal stress directions, the available microstructural experimental data must be appropriately augmented in concert with analyses and macroscopic observations. In non-proportional loading a group of microcracks which were subjected to tension may ultimately find themselves in hydrostatic compression. A sudden reversal of their status from active to passive will result in a discontinuous change of the effective macroparameters. This class of problems can be handled only by the rate theories.

The intricacies of the brittle-ductile transition and the influence of the rock fabric on this transition have been discussed in considerable length in the existing literature (see, for example, Paterson, 1978). Analytical models of this transition are still in their infancy. This is not surprising since the onset of the brittle-ductile transition depends on the microcrack interaction. The extent of the interaction depends on the distance between pairs of microdefects. The largest interaction occurs when the distance between two defects is smallest. In other words, it is the smallest distance rather than the average distance that is of interest. This rather simple conclusion seems to have been totally ignored in most of the literature.

2.2. CYLINDRICAL PORE MODEL

In porous rocks (such as sandstones and limestones), microcrack nucleation is commonly attributed to the local tensile stresses along the pore circumference. The circumferential (hoop) normal stresses along the exterior of a single, circular hole of radius R , embedded in a plate of homogeneous, isotropic, linear elastic material (Fig. 2.1) are

$$\sigma_{\theta} = \frac{1}{2}\sigma^0 \left[1 + \frac{R^2}{r^2} - \left(1 + 3\frac{R^4}{r^4} \right) \cos 2\theta \right], \text{ for } r > R, \quad (2.1)$$

where σ^0 is the magnitude of the macrostress applied in the direction of the x-axis. From (2.1) the extreme values of the stresses at the pore perimeter are

$$\begin{aligned} \sigma_{\theta} &= 3\sigma^0, \text{ for } \theta = \frac{\pi}{2}, r = R \\ \sigma_{\theta} &= -\sigma^0, \text{ for } \theta = 0, r = R. \end{aligned} \quad (2.2)$$

It is trivial to show that the hoop tensile stresses along the pore circumference occur within the range $|\theta| < 30^\circ$. However, the already mentioned observations of Hallbauer, *et al.* (1973) on argillaceous quartzite and the Zheng, *et al.* (1991) measurements on limestone are not in very good agreement with the results predicted by this simple model. According to their observations there are no apparent cracks with orientations larger than (beyond) the angle of $\theta = 15^\circ$. However, a crack nucleated in a plane subtending a large angle to the compression axis will kink and grow along the x-axis (Fig. 2.1). Moreover, the cracks nucleated at $\theta = 0$, $r = R$ will, in general, become unstable before the stress near $\theta = 30^\circ$ becomes large enough to propagate cracks from small notches. Thus, even though some cracks may indeed nucleate from a notch at an angle close to $\theta = 30^\circ$, the average crack density in these planes will be minimal.

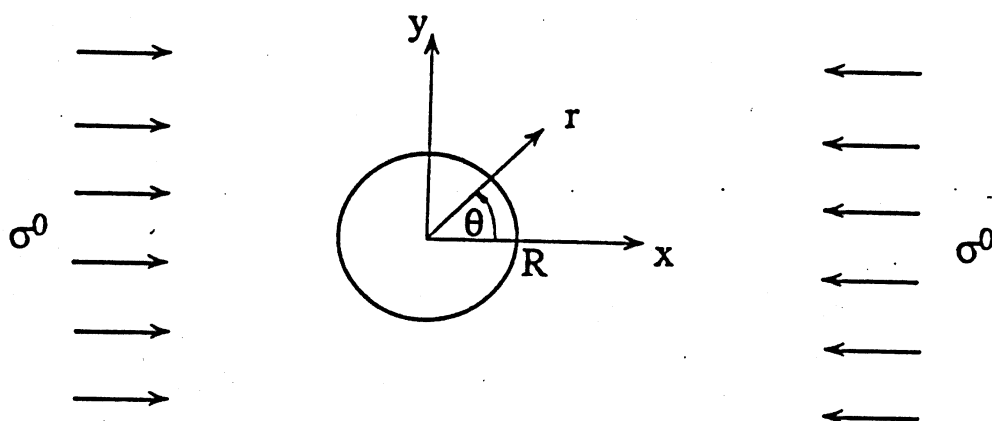


Figure 2.1. Cylindrical pore of radius R under remote compressive stress σ^0 .

In the case of biaxial compression

$$\sigma_x = -\sigma^0 \quad \text{and} \quad \sigma_y = -\varphi \sigma^0, \quad (2.3)$$

where φ is an arbitrary number, and the tensile stresses vanish for $\varphi \geq 1/3$. Thus, according to this simple criterion the microcracks will not nucleate at the perimeter of an isolated cylindrical pore if $\varphi \geq 1/3$. Introducing the average (hydrostatic) stress p and the deviatoric (differential) stress q

$$p = \frac{1}{2}(\sigma_x + \sigma_y), \quad \text{and} \quad q = \frac{1}{2}(\sigma_x - \sigma_y) \quad (2.4)$$

the local tensile stresses will vanish if the ratio

$$\frac{q}{p} = \frac{1-\varphi}{1+\varphi} \leq 1. \quad (2.5)$$

The equality sign in (2.5) provides a simple-minded estimate of the brittle-ductile transition neglecting microdefect interaction, other micromechanical mechanisms, and the three-dimensional character of the phenomenon.

It is also of interest to consider the stress concentrations in the proximity of two interacting cylindrical pores. The available data in Savin (1961) and Paterson (1978) indicate that the stress concentrations are decreased by the presence of the second pore. Detailed rigorous analyses were reported for the case shown in Fig. 2.2 using the elasticity model formulated by Kouris and

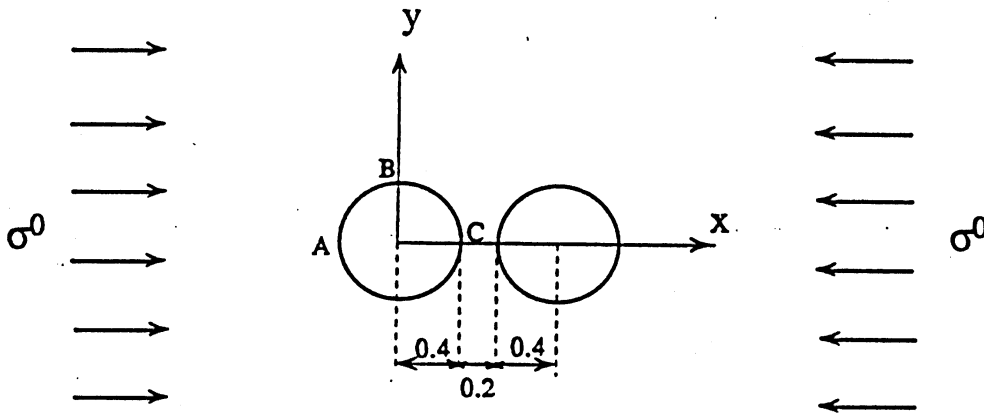


Figure 2.2. Two interacting cylindrical pores under remote compressive stress σ^0 .

Tschucida (1991). The local stresses at points A, B and C are: $\sigma_y^A = 0.903\sigma_0$, $\sigma_x^B = -2.59\sigma_0$, and $\sigma_y^C = 0.38\sigma_0$. The corresponding values for a single pore are 1.0, -3.0, and 1.0, respectively. However, very near the point C, i.e. at $x = 0.41$, the matrix is subjected to biaxial tension $\sigma_x = 0.90\sigma_0$ and $\sigma_y = 0.36\sigma_0$. The performed calculations indicate that the second pore has a shielding effect, and will seldom if ever amplify the stresses determined for a single hole.

Naturally, the perimeter of a void in rock material is never smooth. The void surface is typically irregular, containing small notches and fissures. Thus, to determine the stability of the deformation process it is more appropriate to consider a notched void as shown in Fig. 2.3 (Kemeny and Cook, 1991). When the crack length a is much smaller than the pore radius R , the actual geometry can be approximated by an edge crack. This edge crack is subjected to the local hoop stress computed from (2.2). The stress intensity factor for this case is (Rooke and Cartwright, 1976)

$$K_I = 1.12 (\sigma_x - 3\sigma_y) \sqrt{\pi a}, \quad \sigma_x > 3\sigma_y, \quad a \ll R. \quad (2.6)$$

For longer cracks, Sammis and Ashby (1986) suggested an approximate expression for the stress intensity factor in the form

$$K_I = \sqrt{\alpha} \left[1.1 \frac{1 - 2.1\varphi}{(1 + \alpha)^{3.3}} - \varphi \right] \sigma^0 \sqrt{\pi R}, \quad (2.7)$$

where $\alpha = a/R$. The normalized stress intensity factor $\sigma^0 \sqrt{\pi R}/K_C$, where K_C is the critical stress intensity factor, is plotted in Fig. 2.4 vs. the aspect ratio $\alpha = a/R$, for several different confinement ratios $\varphi = \sigma_y/\sigma_x$. In all cases the maximum stress intensity factor occurs for $a < R$. After the stress reaches maximum, the crack growth becomes unstable (for low confinement) in the sense that the crack length increases for decreasing stress.

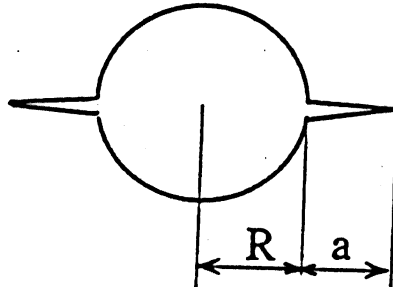


Figure 2.3. A notched void of radius R and crack length a .

Sammis and Ashby (1986) also suggested an approximate expression for the case of interacting cracks. According to this suggestion the total stress intensity factor can be approximated by adding an additional term to (2.7)

$$K_I' = \frac{\sqrt{2}}{\pi} \left\{ \left[1 - \frac{8\varphi}{\pi}(1+\alpha)^3 f \right] \left[1 - \frac{2\varphi}{\pi}(1+\alpha)^3 f \right] f(1+\varphi) \right\}^{1/2} \sigma^0 \sqrt{\pi R} \quad (2.8)$$

reflecting the enhancement attributable to the direct crack interaction. In (2.8), f is used to denote the initial porosity of the rock.

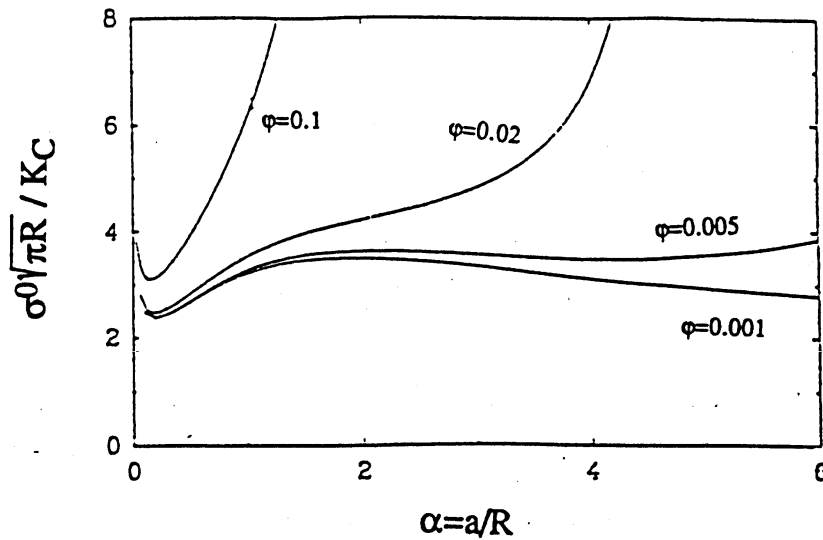


Figure 2.4. Normalized stress-intensity factor vs. aspect ratio a/R , for several different confinement ratios φ .

2.3. BRITTLE-DUCTILE TRANSITION

Using expressions (2.7) and (2.8) the Griffith's stability condition (Kanninen and Popelar, 1985) can be written as

$$K_I + K_I' = K_C, \quad (2.9)$$

where K_C is the critical stress intensity factor considered to be a material parameter. The normalized stress needed to propagate the crack can now be written from the three above

expressions as a function of the length ratio $\alpha = a/R$ and the degree of the lateral confinement $\varphi > 0$. These results (taken from Wong, 1990) are reproduced in Fig. 2.5, and indicate that confinement as low as $\varphi > 0.005$ suffices to render the crack stable. This conclusion, however, contradicts the experimental results referenced in Wong (1990) indicating that the Sammis and Ashby (1986) model overestimates the stabilizing effect of the lateral confining stresses, i.e., that it provides a low estimate of the magnitude of the deviatoric stresses needed to prevent the brittle failure.

Isida and Nemat-Nasser (1987) performed rigorous computations which indicated that the expression (2.9) for the stress-intensity factor overestimates the destabilizing effect of the crack interaction (Wong, 1990). Moreover, the two-dimensional approximation of a three-dimensional problem further exaggerates the influence of the interaction. Thus, even though the Sammis and Ashby (1986) model exaggerates the effect of the crack interaction, it simultaneously overestimates the stabilizing influence of the lateral confinement. Thus, this model leads to a contradictory set of conclusions. Even though their interaction is exaggerated, the cracks are still predicted to grow in a stable mode at minute levels of lateral confinement. This apparent paradox was further discussed in Wong (1990). The influence of the pore shape was shown to be marginal in respect to the determination of the brittle-ductile transition. The stress-intensity factors for a crack emanating from a vertex of a square hole (Hasebe and Ueda, 1980) are indeed larger, but not enough to affect the stability of the crack growth. The expressions for a three-dimensional case of spherical cavities (Sammis and Ashby, 1986) do not change the basic conclusions either. This prompted Wong (1990) to conclude that the "Sammis and Ashby (1986) model is not appropriate for low-porosity rocks", and that "compaction mechanisms (including pore collapse and grain rotation) are probably operative". However, it seems that a critical evaluation of the pore model may furnish a new insight into the phenomenon and provide a better estimate of the brittle-ductile transition.

The Isida and Nemat-Nasser (1987) computations were performed for a perfect, doubly periodic pattern of two cracks emanating from a circular hole. Using these results to explain experimental observations regarding the onset of unstable crack growth implies self-similar growth of defects throughout the deformation process. However, as shown in Bazant, *et al.* (1989) and Bazant and Cedolin (1991) self-similar growth of defects represents a thermodynamically unstable path. This is obvious on purely physical grounds as well. Assuming all distances between adjacent defects to be equal (as implied by the so-called cell method based on doubly periodic patterns) the minimum distance between two defects is obviously maximized. However, the interaction of cracks and the formation of a cluster of cracks depends almost entirely on the minimum (rather than average) distance.

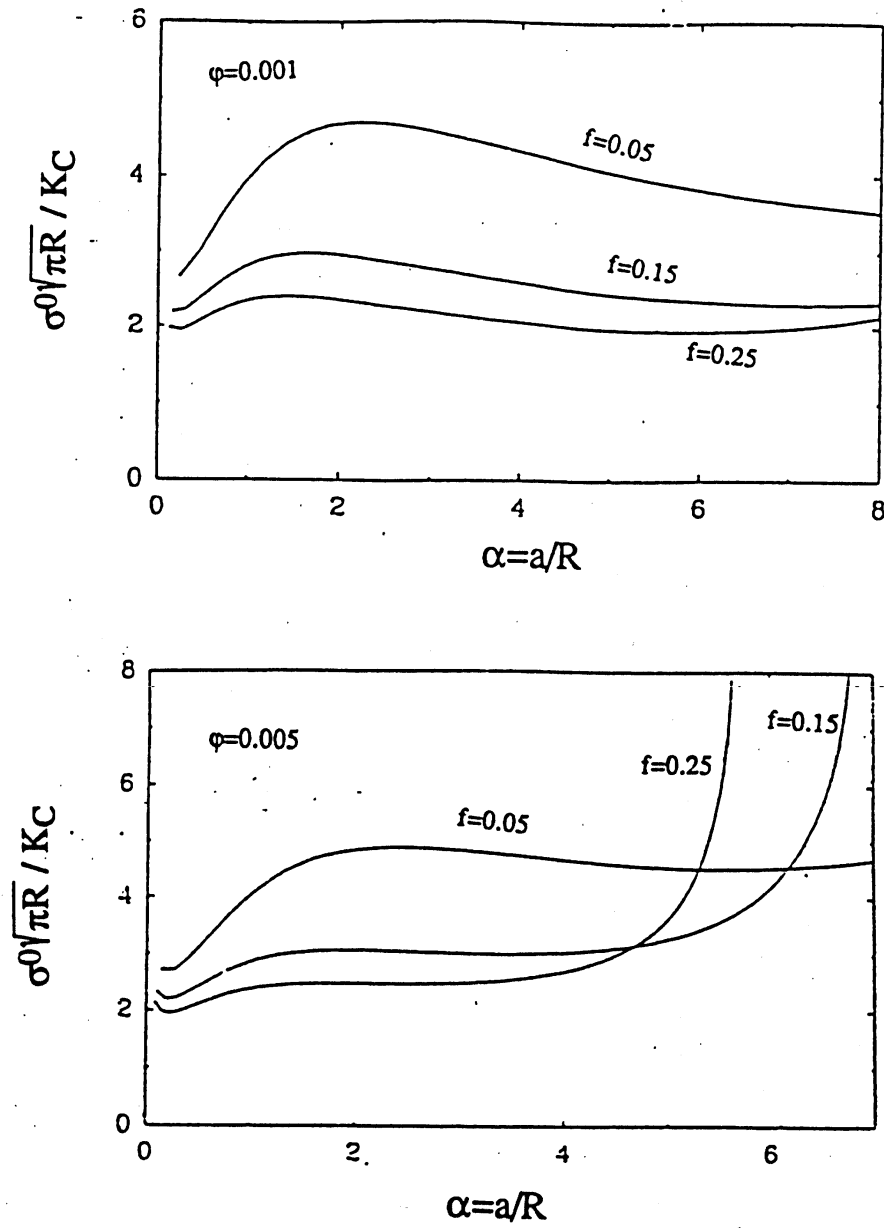


Figure 2.5. Normalized stress-intensity factor vs. aspect ratio a/R , for several different values of porosity f and two confinement ratios φ .

The already mentioned acoustic emission data on sandstones (Lockner, *et al.*, 1992) provides strong evidence that the AE signal clustering characterizes the deformation process from its earliest stages. Most of the signals are strongly clustered indicating strong microcrack interaction. This experimental evidence proves the existence of a basic flaw in the predictions of the cell models which imply preservation of the periodicity of the defect pattern. The assumption that the defect periodicity (microstructural order) perseveres into the latter part of the deformation process dominated by the microdefect interaction, substantially overestimates the ductility and strength and underestimates the onset of brittle instability. This, in fact, renders the cell model inadequate in qualitative and quantitative senses alike. It seems reasonable to acknowledge the dominant role of the clustering, i.e., the spatial disorder of the microstructure. Since the clustering at low density of defects depends on the smallest distance between adjacent cracks, it is important to investigate the effect of the statistical distribution of defect distances on the deformation pattern.

It is important to emphasize that the available experimental data clearly indicate that the onset of the brittle-ductile transition is a statistical event. The emergence of the zone of large microcrack density depends not only on the porosity (first statistical moment of the void distribution), but in a much more substantial manner on the higher, perhaps extreme, statistical moments defining extremes of the pore spacing. Thus, a study similar to one suggested by Horii and Nemat-Nasser (1986) for compact rocks may not provide a reliable estimate. In fact, it seems that every deterministic model based on the average spacing of pores will underestimate the onset of the unstable crack regime.

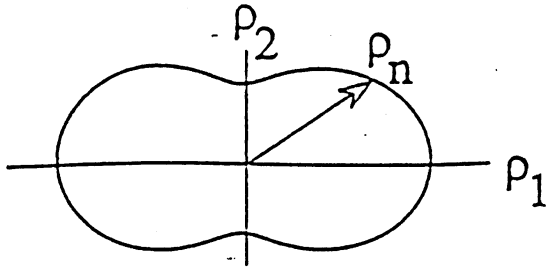
3.0 PHENOMENOLOGICAL DAMAGE MODELS FOR BRITTLE DEFORMATION OF ROCKS

3.1. CRACK DENSITY DISTRIBUTION

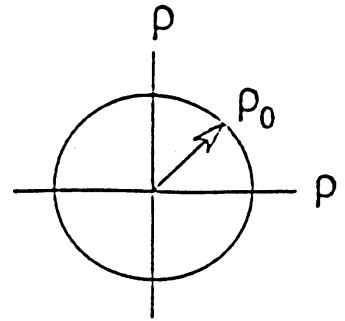
Consider a porous rock specimen containing a certain distribution of microcracks accumulated during a specific loading program from some initial state. Two questions of paramount importance are: a) what are the damage variables that adequately represent the degraded state, and b) how does the elastic stiffness of a damaged rock specimen depend on the introduced damage variables? Regarding the first question, various damage variables have been introduced in the literature. Most of these models are of limited validity. If the current crack pattern in the representative volume element is such that cracks are uniformly distributed in all planes, regardless of their orientation, a scalar damage variable should be a natural choice. The corresponding distribution of damage is referred to as isotropic. If cracks are nonuniformly distributed over differently oriented planes, damage distribution and correspondingly the material response are anisotropic. A distribution function $\rho(n)$ (defined on a unit sphere) can be introduced to define the directional dependence of the crack density. This function can be expanded in a Fourier-type series of certain families of spherical functions (Kanatani, 1984, Onat and Leckie, 1988), containing dyadic products of the unit vector and the Kronecker delta tensor. In addition to the scalar (isotropic) term, the second-, fourth-, and higher even-order symmetric tensors appear in this representation. Therefore, the accurate representation of a complicated, highly anisotropic orientation of damage by introducing some average tensor measure of damage is a difficult task which in general requires introduction of second-, fourth-, and possibly even higher-order tensors to represent the state of damage. An alternative description of damage anisotropy involving stereological measurements and using a geometric probability approach is discussed by Wong (1985).

In a general case of loading of initially anisotropic rocks, the planes containing extreme densities of damage are not mutually perpendicular. Consequently, both the damage itself and its effect on the material's effective stiffness are anisotropic. However, in the case of initially isotropic brittle rocks subjected to proportional loading, the density of damage is maximum in the plane perpendicular to the largest principal tensile stress and minimum in the plane normal to the minimum principal stress. To study this case of damage distribution, it seems reasonable to approximate its density distribution by an oval (Fig. 3.1a). This type of damage distribution can then be represented by a second-order tensor. If ρ_{ij} denotes the components of the second-order crack density tensor ρ , the density of cracks embedded in the planes with a normal n is given by

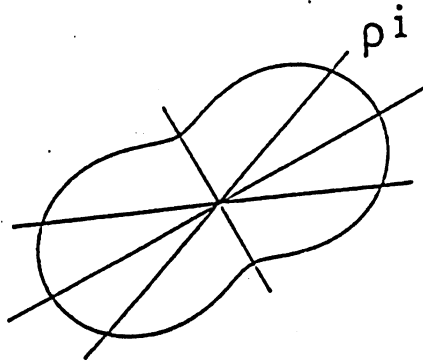
$$\rho(n) = \rho_{kl} n_k n_l, \quad (3.1)$$



(a)



(b)



(c)

Figure 3.1. (a) Crack distribution within orthogonal crack families modeled by a continuous crack distribution of oval shape; (b) If the crack densities are the same, the oval shape becomes spherical, giving rise to an isotropic damage distribution; (c) Crack distribution corresponding to inclined crack families.

depicted by the oval shape of Fig. 3.1a. Multiplying (3.1) with $n_i n_j$ and integrating over all directions spanning the entire solid angle $\Omega = 4\pi$, and using

$$\int_{4\pi} n_i n_j n_k n_l d\Omega = \frac{4\pi}{15} (\delta_{ik} \delta_{jl} + \delta_{il} \delta_{jk} + \delta_{ij} \delta_{kl}) ,$$

it follows that

$$\frac{8\pi}{15} (\rho_{ij} + \frac{1}{2} \rho_{kk} \delta_{ij}) = \int_{4\pi} \rho(n) n_i n_j d\Omega . \quad (3.2)$$

Above, δ_{ij} denotes the Kronecker delta. The contraction $i = j$ in (3.2) defines the first invariant of the crack density tensor

$$\rho_{kk} = \frac{3}{4\pi} \int_{4\pi} \rho(n) d\Omega . \quad (3.3)$$

Substituting (3.3) into (3.2), the crack density tensor can be expressed as

$$\rho_{ij} = \frac{15}{8\pi} (\mathcal{D}_{ij} - \frac{1}{5} \rho_0 \delta_{ij}) . \quad (3.4)$$

In (3.4)

$$\rho_0 = \int_{4\pi} \rho(n) d\Omega \quad (3.5)$$

is the density of all cracks within a unit volume, and

$$\mathcal{D}_{ij} = \int_{4\pi} \rho(n) n_i n_j d\Omega \quad (3.6)$$

is a second-order tensor which shall be referred to as a damage tensor. The corresponding damage distribution is orthotropic. If the distribution is isotropic, so that $\rho(n) = \rho_0/4\pi = \text{constant}$, (3.6) reduces to $\mathcal{D}_{ij} = \frac{1}{3} \rho_0 \delta_{ij}$, while the crack density tensor (3.4) becomes $\rho_{ij} = \frac{1}{4\pi} \rho_0 \delta_{ij}$. The oval shape of Fig. 3.1a then transforms to a spherical shape (Fig. 3.1b).

In two-dimensional problems one has

$$\int_{2\pi} n_i n_j n_k n_l d\Omega = \frac{2\pi}{8} (\delta_{ik} \delta_{jl} + \delta_{il} \delta_{jk} + \delta_{ij} \delta_{kl}) ,$$

so that, in place of (3.4), the crack density tensor is given by

$$\rho_{ij} = \frac{2}{\pi}(\mathcal{D}_{ij} - \frac{1}{4}\rho_0 \delta_{ij}) . \quad (3.4')$$

Higher-order tensors are needed to accurately represent the general cases of crack distributions, especially when the damage is not orthotropic. For example, the fourth-order crack density tensor $\bar{\rho}_{ijkl}$ describes the crack density corresponding to planes with a normal \mathbf{n} as

$$\rho(\mathbf{n}) = \bar{\rho}_{ijkl} n_i n_j n_k n_l . \quad (3.7)$$

The second-order damage tensor is still defined by (3.6), while the fourth-order damage tensor is defined by

$$\bar{\mathcal{D}}_{ijkl} = \int_{4\pi} \rho(\mathbf{n}) n_i n_j n_k n_l d\Omega . \quad (3.8)$$

The relationship between the fourth-order crack density tensor $\bar{\rho}$ and the second- and fourth-order damage tensors \mathcal{D} and $\bar{\mathcal{D}}$ can be derived by a similar procedure as (3.4). It follows that

$$\bar{\rho}_{ijkl} = \frac{315}{32\pi}(\bar{\mathcal{D}}_{ijkl} - \frac{2}{3}\mathcal{A}_{ijkl} + \frac{1}{21}\rho_0 \mathcal{B}_{ijkl}) , \quad (3.8')$$

where:

$$\mathcal{A}_{ijkl} = \frac{1}{6}(\delta_{ij}\mathcal{D}_{kl} + \delta_{kl}\mathcal{D}_{ij} + \delta_{ik}\mathcal{D}_{jl} + \delta_{il}\mathcal{D}_{jk} + \delta_{jk}\mathcal{D}_{il} + \delta_{jl}\mathcal{D}_{ik})$$

$$\mathcal{B}_{ijkl} = \frac{1}{3}(\delta_{ij}\delta_{kl} + \delta_{ik}\delta_{jl} + \delta_{il}\delta_{jk}) .$$

In two dimensions, expression (3.8') is replaced by

$$\bar{\rho}_{ijkl} = \frac{8}{\pi}(\bar{\mathcal{D}}_{ijkl} - \frac{3}{4}\mathcal{A}_{ijkl} + \frac{1}{16}\rho_0 \mathcal{B}_{ijkl}) . \quad (3.8'')$$

3.1.1. Second- And Fourth-Order Approximations

To illustrate application of the results from Section 3.1, consider first the case of two orthogonal crack families, each having the crack density $\rho_0/2$. In a two-dimensional analysis this crack distribution can be represented by

$$\rho(\theta) = \frac{\rho_0}{4}[\delta(\theta) + \delta(\theta - \frac{\pi}{2}) + \delta(\theta - \pi) + \delta(\theta - \frac{3\pi}{2})] , \quad (a)$$

where θ defines an arbitrary direction through the point under consideration, and δ denotes the Dirac delta function. Substituting (a) into the expression for the second-order damage tensor

$$\mathcal{D}_{ij} = \int_{2\pi} \rho(n) n_i n_j d\Omega, \quad (3.6')$$

it follows that $\mathcal{D}_{ij} = \frac{1}{2} \rho_0 \delta_{ij}$. Hence, from (3.4') the crack density tensor is $\rho_{ij} = \frac{1}{2\pi} \rho_0 \delta_{ij}$, so that within the second-order approximation (3.1), the distribution (a) is replaced by the continuous distribution

$$\rho(\theta) = \rho_{ij} n_i n_j = \frac{1}{2\pi} \rho_0, \quad (b)$$

i.e., the circle of radius $\rho_0/2\pi$. Therefore, two orthogonal crack families with the same crack densities are replaced by an isotropic homogeneous crack distribution.

A more accurate approximation is obtained using the fourth-order damage tensor. Substituting (a) into (3.8), it follows that $\bar{\mathcal{D}}_{1111} = \bar{\mathcal{D}}_{2222} = \rho_0/2$, while all others components are equal to zero. The tensor \mathcal{A} has the components $\mathcal{A}_{1111} = \mathcal{A}_{2222} = \rho_0/2$, and $\mathcal{A}_{1122} = \mathcal{A}_{2211} = \mathcal{A}_{1212} = \mathcal{A}_{2121} = \mathcal{A}_{1221} = \mathcal{A}_{2112} = \rho_0/6$, as the only non-zero components. Substitution into (3.8'') and

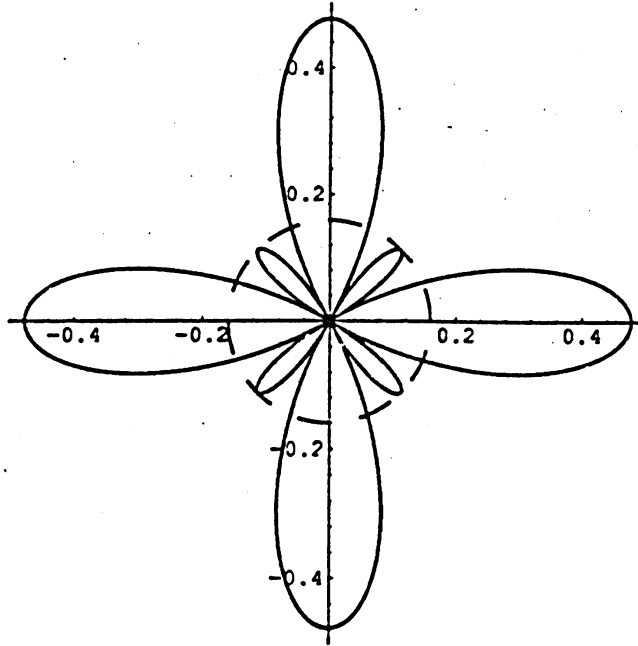


Figure 3.2. Second- and fourth-order continuous approximations of two orthogonal crack families with the same crack densities.

(3.7), therefore, gives the continuous fourth-order approximation

$$\rho(\theta) = \bar{\rho}_{ijkl} n_i n_j n_k n_l = \frac{1}{2\pi} \rho_0 (1 + 2\cos 4\theta) . \quad (c)$$

The second- and fourth-order continuous approximations (b) and (c) are plotted in Fig. 3.2. A remarkable feature of the fourth-order approximation in this case is that, in addition to dominating regions of positive crack density, two orthogonal regions of negative crack density also occur, at 45° relative to the positive regions. This can even happen within the second-order approximation, as will be discussed in the next subsection.

3.1.2. *Negative Crack Density—Anticracks*

The observed feature of negative crack density often occurs when the actual crack distribution is approximated by a continuous distribution corresponding to second-, fourth- or higher-order damage tensors. To illustrate this, consider a single family of cracks whose normal is $\mathbf{n} = \{0, 1\}$, written in a symmetrical form as

$$\rho(\theta) = \frac{\rho_0}{2} [\delta(\theta - \frac{\pi}{2}) + \delta(\theta - \frac{3\pi}{2})] . \quad (d)$$

The continuous approximation of this distribution, corresponding to the use of the second-order damage tensor, is

$$\rho(\theta) = \frac{1}{2\pi} \rho_0 (1 - 2 \cos 2\theta) . \quad (e)$$

Derivation of the above expression is identical to one already explained in Section 3.1.1. The graphical depiction of the second-order tensor approximation is shown in Fig. 3.3. The interesting feature of this continuous distribution is emergence of the negative crack density over a part of the range. This means that in the corresponding regions, actual cracks are replaced by rigid lamella (the opposite of a crack) which are referred to as negative cracks or anticracks (Dundurs and Markenscoff, 1989). The emergence of negative crack densities as a result of approximating discontinuous distributions of cracks by continuous distributions represented by tensors, should have been expected. A tensorial approximation (e) of a delta function implies the existence of damage at angles other than $\theta = \pi/2$ and $\theta = 3\pi/2$. Consequently, negative crack densities must be present to balance this nonexistent damage.

The regions with negative crack density and corresponding anticrack distributions, also occur when the fourth-order approximation is used. In this case one has

$$\rho(\theta) = \frac{1}{2\pi} \rho_0 (1 - 2 \cos 2\theta + 2 \cos 4\theta) . \quad (f)$$

The plot of this density distribution, with its regions of negative crack density, is shown in Fig. 3.3 (dashed curve). The actual crack distribution is approximated much better than in the case of the second-order tensor.

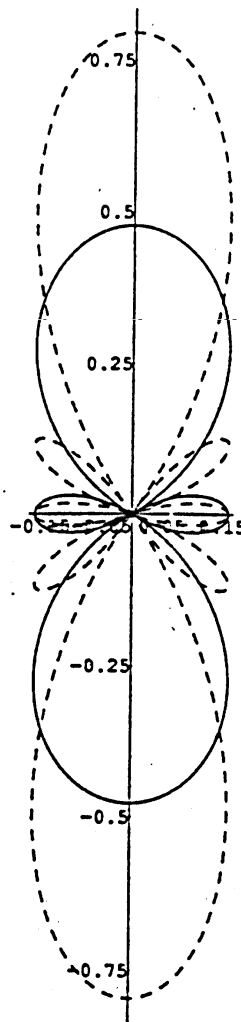


Figure 3.3. Second- and fourth-order continuous approximations of a single crack family.

Of course, in many cases the approximate continuous crack distribution does not contain regions of negative crack density. For example, for two orthogonal crack families with crack densities ρ_1 and $\rho_2 = \rho_0 - \rho_1$, where ρ_0 is the total crack density, the occurrence of regions with negative crack densities depends on the ratio ρ_1/ρ_0 . If $\rho_1 = \rho_0/8$ and $\rho_2 = 7\rho_0/8$, the density distribution according to the second-order approximation is

$$\rho(\theta) = \frac{1}{2\pi}\rho_0\left(1 - \frac{3}{2}\cos 2\theta\right).$$

Thus, the negative crack density regions occur again, as shown in Fig. 3.4a. However, if $\rho_1 = \rho_0/3$ and $\rho_2 = 2\rho_0/3$, the crack density distribution is

$$\rho(\theta) = \frac{1}{2\pi}\rho_0\left(1 - \frac{2}{3}\cos 2\theta\right),$$

showing no regions of negative crack density (Fig. 3.4b). The transition case is $\rho_1 = \rho_0/4$ and $\rho_2 = 3\rho_0/4$, for which

$$\rho(\theta) = \frac{1}{2\pi}\rho_0(1 - \cos 2\theta),$$

(see Fig. 3.4c).

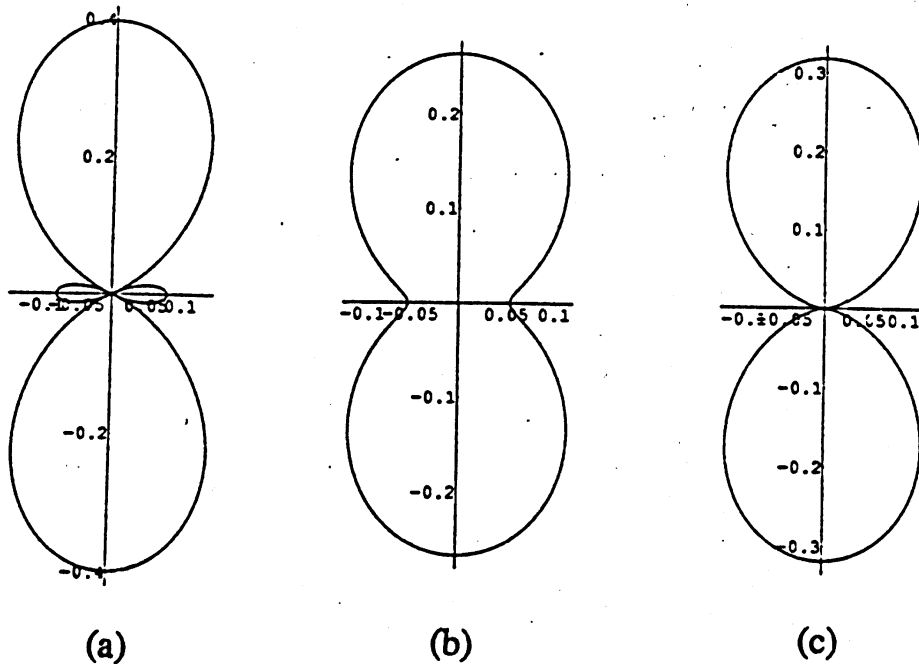


Figure 3.4. Continuous crack distributions corresponding to two orthogonal crack families of different crack density ratios.

3.1.3. Rose Diagram

The same procedure applies in approximating an arbitrary, experimentally measured crack distribution by a continuous distribution, based on the even-order tensor measures. Consider for example a "rose diagram" deduced from the actual measurements in tests performed by Hallbauer, *et al.* (1973), Fig. 3.5a. Using the second-order tensor approximation, the components of the corresponding damage tensor are calculated from (3.6') with $n = \{\cos\theta, \sin\theta\}$ to be : $\mathcal{D}_{11} = 0.061\rho_0$, $\mathcal{D}_{22} = 0.939\rho_0$ and $\mathcal{D}_{12} = 0.111\rho_0$. Consequently, substituting these results into (3.4') the components of the crack density tensor are computed to be: $\rho_{11} = -\frac{1}{2\pi}0.75\rho_0$, $\rho_{22} = \frac{1}{2\pi}2.75\rho_0$, and $\rho_{12} = \frac{1}{2\pi}0.44\rho_0$. Therefore, the approximate continuous crack distribution is given by

$$\rho(\theta) = \frac{1}{2\pi}\rho_0(-0.75 \cos^2\theta + 2.75 \sin^2\theta + 0.44 \sin\theta\cos\theta) ,$$

i.e.,

$$\rho(\theta) = \frac{1}{2\pi}\rho_0(1 + 0.22 \sin 2\theta - 1.75 \cos 2\theta) .$$

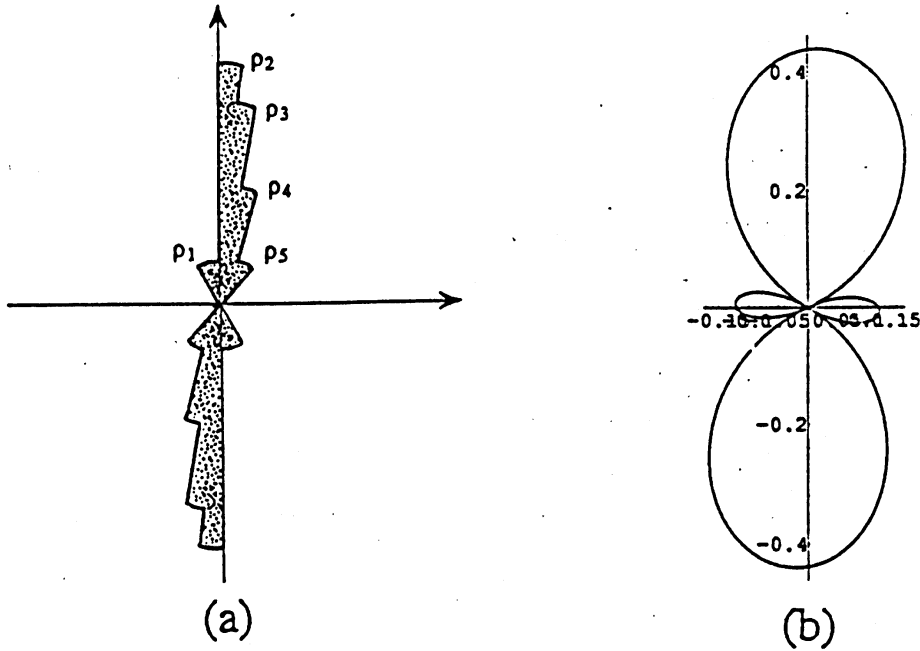


Figure 3.5. (a) A "rose diagram" deduced from actual test measurements. The representative crack densities are: $\rho_1 = \rho_5 = 1.8\rho_0/2\pi$, $\rho_2 = 14.4\rho_0/2\pi$, $\rho_3 = 10.8\rho_0/2\pi$, and $\rho_4 = 7.2\rho_0/2\pi$, where ρ_0 is the total crack density; (b) Continuous second-order approximation for crack density distribution corresponding to the above "rose diagram".

This approximate crack distribution is plotted in Fig. 3.5b. In addition to the dominating regions of positive crack density, the regions of negative crack density are still present. The scalar (isotropic) approximation is a circle of radius $\rho_0/2\pi$. This phenomenon, as yet not discussed in the literature, deserves careful consideration. This is especially true since negative crack densities actually do occur in analyzing situations such as those studied by Hallbauer, *et al.* (1973).

3.2. REPRESENTATION OF DAMAGE

To illustrate a class of relatively simple representations of damage, consider an initially isotropic, homogeneous and elastic matrix subjected to proportional loading. According to the experimental data on rocks (Hallbauer, *et al.*, 1973, or Zheng, *et al.*, 1991) the planes of extreme microcrack density coincide with the principal planes of the stress tensor. Consequently, the specimen is orthotropic on the macroscopic scale suggesting that the microcrack distribution can be represented by the second-order damage tensor (Vakulenko and Kachanov, 1971, Kachanov, 1980, etc.)

$$\mathcal{D} = \rho_n \mathbf{N} + \rho_m \mathbf{M} + \rho_k \mathbf{K}, \quad (3.9)$$

where $\mathbf{N} = \mathbf{n} \otimes \mathbf{n}$, $\mathbf{M} = \mathbf{m} \otimes \mathbf{m}$ and $\mathbf{K} = \mathbf{k} \otimes \mathbf{k}$ are the dyadic products, and \mathbf{n} , \mathbf{m} and \mathbf{k} are the unit normals to three crack families. The scalar quantities ρ_n , ρ_m and ρ_k are the corresponding crack densities.

Experimental determination of crack densities involves a micro-to-macro transition. This implies the existence of a representative volume element centered at a point, which contains a statistically valid sample of microcracks influencing the state at the considered point. Thus, if within a material element of unit volume there are N parallel flat cracks with the unit normal \mathbf{n} and an average characteristic length a , the nondimensional crack density is defined as $\rho_n = Na^3$. The crack length a is calculated as an average characteristic length of all cracks within a representative volume element, imbedded on planes with the normal \mathbf{n} .

The minimum prescription for representation (3.9), based in equal parts on intuition and experimental data, is to measure microcrack densities ρ_n , ρ_m and ρ_k in three principal planes. Naturally, there is no assurance that the estimate of microcrack density in an arbitrary plane, interpolated using the representation (3.9), will coincide with the actual density. Indeed, the representation of the damage distribution by the second-order tensor (3.9) amounts to assuming a continuous crack distribution of the oval type shown in Fig. 3.1a, with appropriately adjusted crack densities (preserving as constant the total number of cracks in a unit volume, i.e. $\rho_n + \rho_m + \rho_k = \rho$, given by (3.5)). If $\rho_n = \rho_m = \rho_k = \rho_0$, the oval shape becomes a sphere (of radius $3\rho_0/4\pi$). Therefore, within a description by the second-order damage tensor,

the three orthogonal crack families with the same crack densities give rise to an isotropic damage distribution (Fig. 3.1b).

A more ambitious alternative consists of measuring microcrack densities ρ^i in a large number of planes with different orientations \mathbf{n}^i , in order to form a "rose" histogram (Kanatani, 1984). In this case the second-order representation (3.9), in which ρ_n , ρ_m and ρ_k are the principal values, and \mathbf{n} , \mathbf{m} and \mathbf{k} are the principal directions of the second-order tensor $\sum_i \rho^i \mathbf{n}^i \otimes \mathbf{n}^i$, may or may not be a satisfactory approximation of the measured data. Geometrically, the approximation (3.9) again amounts to replacing a more complicated distribution (such as the one shown in Fig. 3.1c) by an oval ("orthotropic") distribution.

Since $N + M + K = 1$, (3.9) can be rewritten as

$$\mathcal{D} = (\rho_n - \rho_k)N + (\rho_m - \rho_k)M + \rho_k \mathbf{1}, \quad (3.10)$$

where $\mathbf{1}$ denotes the second-order unit tensor. Two special cases of (3.10) are of interest. If $\rho_k = \rho_m \neq \rho_n$ (transversely isotropic case), the damage tensor (3.10) simplifies to

$$\mathcal{D} = (\rho_n - \rho_m)N + \rho_m \mathbf{1}. \quad (3.11)$$

In the isotropic case, $\rho_n = \rho_m = \rho_k = \rho$, and (3.11) reduces to a spherical tensor $\mathcal{D} = \rho \mathbf{1}$, describing an isotropic damage distribution.

3.3. ELASTIC STIFFNESS TENSOR

In the considered brittle deformation processes, the state of the material is locally defined by two state variables: elastic strain \mathbf{E}_e and the damage tensor \mathcal{D} . The second of these variables is often referred to as the internal or hidden variable. The elastic free energy ψ_e is, therefore, $\psi_e = \psi_e(\mathbf{E}_e, \mathcal{D})$. This expression must be invariant with respect to any change of reference frame. Since under the change of frame defined by an orthogonal transformation \mathbf{Q} , the damage tensor \mathcal{D} becomes $\mathbf{Q}\mathcal{D}\mathbf{Q}^T$ (superscript T denotes the transpose), the invariance condition requires the elastic free energy ψ_e to be an isotropic function of both elastic strain \mathbf{E}_e and damage \mathcal{D} . According to the well known invariance theorem (Spencer, 1971), an isotropic scalar function of two symmetric second-order tensor variables can be represented as a polynomial of its irreducible integrity basis:

$$(\mathbf{E}_e : \mathbf{1}), (\mathbf{E}_e : \mathbf{E}_e), (\mathbf{E}_e^2 : \mathbf{E}_e), (\mathcal{D} : \mathbf{1}), (\mathcal{D} : \mathcal{D}), (\mathcal{D}^2 : \mathcal{D}) \\ (\mathbf{E}_e : \mathcal{D}), (\mathbf{E}_e : \mathcal{D}^2), (\mathbf{E}_e^2 : \mathcal{D}), (\mathbf{E}_e^2 : \mathcal{D}^2).$$

In the case of brittle deformation processes, the elastic strains are typically infinitesimal. Moreover, it will be assumed that the stress is equal to zero when the elastic strain vanishes. Thus, the elastic free energy is a quadratic function of the strain components

$$\begin{aligned}\psi_e = & \eta_1(\mathbf{E}_e : \mathbf{E}_e) + \eta_2(\mathbf{E}_e : \mathbf{1})^2 + \eta_3(\mathbf{E}_e : \mathbf{1})(\mathbf{E}_e : \mathcal{D}) + \eta_4(\mathbf{E}_e^2 : \mathcal{D}) \\ & + \eta_5(\mathbf{E}_e^2 : \mathcal{D}^2) + \eta_6(\mathbf{E}_e : \mathcal{D})^2 + \eta_7(\mathbf{E}_e : \mathcal{D}^2)^2.\end{aligned}\quad (3.12)$$

In (3.12), η_i ($i = 1, 2, 3, 4$) are the constants or, more generally, the scalar functions of the invariants of \mathcal{D} . Using (3.12) and the expression $\sigma = \partial\psi_e/\partial\mathbf{E}_e$, the stress-strain relationship acquires the following form

$$\begin{aligned}\sigma = & 2\eta_1\mathbf{E}_e + 2\eta_2(\mathbf{E}_e : \mathbf{1})\mathbf{1} + \eta_3[(\mathbf{E}_e : \mathcal{D})\mathbf{1} + (\mathbf{E}_e : \mathbf{1})\mathcal{D}] + \eta_4(\mathbf{E}_e \cdot \mathcal{D} + \mathcal{D} \cdot \mathbf{E}_e) \\ & + \eta_5(\mathbf{E}_e \cdot \mathcal{D}^2 + \mathcal{D}^2 \cdot \mathbf{E}_e) + 2\eta_6(\mathbf{E}_e : \mathcal{D})\mathcal{D} + 2\eta_7(\mathbf{E}_e : \mathcal{D}^2)\mathcal{D}^2.\end{aligned}\quad (3.13)$$

Above, (\cdot) denotes the inner tensor product. Expression (3.13) is clearly linear in strain, admitting the familiar form

$$\sigma = \mathcal{L}_e(\mathcal{D}) : \mathbf{E}_e. \quad (3.14)$$

The Cartesian components of the instantaneous elastic stiffness tensor \mathcal{L}_e , written in the symmetricized form, are

$$\begin{aligned}\mathcal{L}_{ijkl}^e = & \eta_1(\delta_{ik}\delta_{jl} + \delta_{il}\delta_{jk}) + 2\eta_2\delta_{ij}\delta_{kl} + \eta_3(\delta_{ij}\mathcal{D}_{kl} + \mathcal{D}_{ij}\delta_{kl}) \\ & + \frac{1}{2}\eta_4(\delta_{ik}\mathcal{D}_{jl} + \mathcal{D}_{ik}\delta_{jl} + \delta_{il}\mathcal{D}_{jk} + \mathcal{D}_{il}\delta_{jk}) \\ & + \frac{1}{2}\eta_5(\delta_{ik}\mathcal{D}_{jq}\mathcal{D}_{ql} + \mathcal{D}_{iq}\mathcal{D}_{qk}\delta_{jl} + \delta_{il}\mathcal{D}_{jq}\mathcal{D}_{qk} + \mathcal{D}_{iq}\mathcal{D}_{ql}\delta_{jk}) \\ & + 2\eta_6\mathcal{D}_{ij}\mathcal{D}_{kl} + 2\eta_7\mathcal{D}_{ip}\mathcal{D}_{pj}\mathcal{D}_{kq}\mathcal{D}_{ql}.\end{aligned}\quad (3.15)$$

In (3.15), δ_{ij} denotes the Kronecker delta, i.e., the components of the second-order unit tensor $\mathbf{1}$. Repeated indices indicate summation. Expression (3.15) possesses the obvious symmetries $\mathcal{L}_{ijkl}^e = \mathcal{L}_{jikl}^e = \mathcal{L}_{ijlk}^e$, as well as the self-adjoint symmetry $\mathcal{L}_{ijkl}^e = \mathcal{L}_{klij}^e$. Hence, the elastic strain energy (3.12) can be written as

$$\psi_e = \frac{1}{2}\mathcal{L}_e(\mathcal{D}) : (\mathbf{E}_e \otimes \mathbf{E}_e). \quad (3.16)$$

Consider the case when the damage tensor is defined by (3.11). Since $N_{ik}N_{kj} = N_{ij} = n_in_j$ and $N_{kk} = n_k n_k = 1$, it follows that:

$$\delta_{ij}\mathcal{D}_{kl} + \mathcal{D}_{ij}\delta_{kl} = 2\rho_m I_{ijkl}^2 + \Delta\rho (I_{ijkl}^3 + I_{ijkl}^4)$$

$$\delta_{ik}\mathcal{D}_{jl} + \mathcal{D}_{ik}\delta_{jl} + \delta_{il}\mathcal{D}_{jk} + \mathcal{D}_{il}\delta_{jk} = 4\rho_m I_{ijkl}^1 + 4\Delta\rho I_{ijkl}^5$$

$$\delta_{ik}\mathcal{D}_{jq}\mathcal{D}_{ql} + \mathcal{D}_{iq}\mathcal{D}_{qk}\delta_{jl} + \delta_{il}\mathcal{D}_{jq}\mathcal{D}_{qk} + \mathcal{D}_{iq}\mathcal{D}_{ql}\delta_{jk} = 4\rho_m^2 I_{ijkl}^1 + 4(2\rho_m + \Delta\rho)\Delta\rho I_{ijkl}^5$$

$$\mathcal{D}_{ij}\mathcal{D}_{kl} = \rho_m^2 I_{ijkl}^2 + \rho_m\Delta\rho (I_{ijkl}^3 + I_{ijkl}^4) + (\Delta\rho)^2 I_{ijkl}^6$$

$$\mathcal{D}_{ip}\mathcal{D}_{pj}\mathcal{D}_{kq}\mathcal{D}_{ql} = \rho_m^4 I_{ijkl}^2 + \rho_m^2(2\rho_m + \Delta\rho)\Delta\rho (I_{ijkl}^3 + I_{ijkl}^4) + (2\rho_m + \Delta\rho)^2(\Delta\rho)^2 I_{ijkl}^6,$$

where $\Delta\rho = \rho_n - \rho_m$. The tensors:

$$\begin{aligned} I_{ijkl}^1 &= \frac{1}{2}(\delta_{ik}\delta_{jl} + \delta_{il}\delta_{jk}), & I_{ijkl}^2 &= \delta_{ij}\delta_{kl} \\ I_{ijkl}^3 &= \delta_{ij}n_k n_l, & I_{ijkl}^4 &= n_i n_j \delta_{kl} \\ I_{ijkl}^5 &= \frac{1}{4}(\delta_{ik}n_j n_l + n_i n_k \delta_{jl} + \delta_{il}n_j n_k + n_i n_l \delta_{jk}), & I_{ijkl}^6 &= n_i n_j n_k n_l \end{aligned} \quad (3.17)$$

combining dyadic (tensor) products of the Kronecker delta and a unit vector, form the integrity basis for the fourth-order tensors that are symmetric with respect to the first and second pair of indices (Kunin, 1983). The linear tensor space spanned by this basis is closed with respect to the trace product, forming an algebra. For example, it can be shown that $I^3 : I^2 = I^2$, $I^4 : I^2 = 3I^4$, $I^5 : I^2 = I^4$ and $I^6 : I^2 = I^4$. Hence, the stiffness tensor (3.15) can be written as

$$\begin{aligned} \mathcal{L}_e &= 2(\eta_1 + \eta_4\rho_m + \eta_5\rho_m^2) I^1 + 2(\eta_2 + \eta_3\rho_m + \eta_6\rho_m^2 + \eta_7\rho_m^4) I^2 \\ &\quad + [\eta_3 + 2\eta_6\rho_m + 2\eta_7\rho_m^2(2\rho_m + \Delta\rho)]\Delta\rho (I^3 + I^4) \\ &\quad + 2[\eta_4 + \eta_5(2\rho_m + \Delta\rho)]\Delta\rho I^5 + 2[\eta_6 + \eta_7(2\rho_m + \Delta\rho)^2](\Delta\rho)^2 I^6. \end{aligned} \quad (3.18)$$

3.3.1. Isotropic Damage

Consider first the special case of isotropic damage. In this case the damage is fully defined by a single scalar variable, i.e., $\mathcal{D}_{ij} = \mathcal{D} \delta_{ij}$, where \mathcal{D} is the crack density in each plane. Geometrically, the oval distribution of Fig. 3.1a reduces to a spherical distribution. Since the crack density does not depend on the orientation of the plane, $\rho_n = \rho_m = \rho$ and $\Delta\rho = 0$, and the stiffness tensor (3.18) reduces to a simple form

$$\mathcal{L}_e = 2(\eta_1 + \eta_4\rho + \eta_5\rho^2) \mathbf{I}^1 + 2(\eta_2 + \eta_3\rho + \eta_6\rho^2 + \eta_7\rho^4) \mathbf{I}^2 . \quad (3.19)$$

Neglecting the term proportional to ρ^4 , i.e. taking $\eta_7 = 0$, and introducing the notations:

$$\begin{aligned} \eta_1 = \eta_5 = \mu_0 , \quad \eta_4 = -2\mu_0 \\ \eta_2 = \eta_6 = \lambda_0/2 , \quad \eta_3 = -\lambda_0 \end{aligned} \quad (3.20)$$

where λ_0 and μ_0 are the Lamé elasticity constants of the undamaged material, (3.19) becomes

$$\mathcal{L}_e = (1 - \rho)^2 (2\mu_0 \mathbf{I}^1 + \lambda_0 \mathbf{I}^2) = (1 - \rho)^2 \mathcal{L}_e^0 . \quad (3.21)$$

In (3.21), $\mathcal{L}_e^0 = 2\mu_0 \mathbf{I}^1 + \lambda_0 \mathbf{I}^2$ is the stiffness of the virgin material. Defining $\omega = (1 - \rho)^2$ as the new damage variable, (3.21) takes the form of the familiar representation of the isotropically degraded elastic stiffness, $\mathcal{L}_e = \omega \mathcal{L}_e^0$, originally proposed by Kachanov (1958) and considered at length by Lemaitre (1987, 1992).

In this case the damage distribution is fully defined by a single parameter ρ . This parameter can be readily measured by comparing slopes of the unloading segments of the stress-strain curves.

3.3.2. Transversely Isotropic Damage

If the crack distribution is not isotropic, but approximated by a second-order damage tensor \mathcal{D} , the parameters η_i defined by (3.20) should be accordingly adjusted, in concert with the experimental data for the particular material and crack arrangement. In the sequel, however, the material response will be approximated by the stiffness tensor (3.18) and parameters η_i given by (3.20). Hence

$$\begin{aligned} \mathcal{L}_e = (1 - \rho_m)^2 (2\mu_0 \mathbf{I}^1 + \lambda_0 \mathbf{I}^2) - (1 - \rho_m)\Delta\rho \lambda_0 (\mathbf{I}^3 + \mathbf{I}^4) \\ - [2(1 - \rho_m) - \Delta\rho]\Delta\rho 2\mu_0 \mathbf{I}^5 + (\Delta\rho)^2 \lambda_0 \mathbf{I}^6 \end{aligned} \quad (3.22)$$

defines the elastic stiffness tensor of the considered transversely isotropic material, whose axis of rotational symmetry is parallel to the direction \mathbf{n} . In this case two parameters define the damage distribution: ρ_m and $\Delta\rho = \rho_n - \rho_m$.

If the crack densities are sufficiently small, rendering the terms containing the square of the crack densities negligible, (3.22) reduces to

$$\mathcal{L}_e = \mathcal{L}_e^0 - 2\rho_m (2\mu_0 \mathbf{I}^1 + \lambda_0 \mathbf{I}^2) - \Delta\rho \lambda_0 (\mathbf{I}^3 + \mathbf{I}^4) - 4\Delta\rho \mu_0 \mathbf{I}^5 . \quad (3.23)$$

Finally, if all cracks are embedded in planes parallel to \mathbf{n} ($\rho_n = 0$, $\Delta\rho = -\rho_m$), (3.23) becomes

$$\mathcal{L}_e = \mathcal{L}_e^0 - \rho_m [4\mu_0 \mathbf{I}^1 + 2\lambda_0 \mathbf{I}^2 - \lambda_0 (\mathbf{I}^3 + \mathbf{I}^4) - 4\mu_0 \mathbf{I}^5] . \quad (3.24)$$

3.4. ELASTIC COMPLIANCE TENSOR

To invert the elastic stiffness tensor, expression (3.22) must first be rewritten as

$$\mathcal{L}_e = \sum_{i=1}^6 a_i \mathbf{I}^i , \quad (3.25)$$

where the scalar parameters:

$$\begin{aligned} a_1 &= 2\mu_0(1 - \rho_m)^2 , & a_2 &= \lambda_0(1 - \rho_m)^2 \\ a_3 &= -\lambda_0 (1 - \rho_m)\Delta\rho , & a_4 &= -\lambda_0 (1 - \rho_m)\Delta\rho \\ a_5 &= -2\mu_0 [2(1 - \rho_m) - \Delta\rho]\Delta\rho & a_6 &= \lambda_0 (\Delta\rho)^2 \end{aligned} \quad (3.26)$$

depend only on the material properties of the undamaged material (λ_0, μ_0) and the densities of the already accumulated damage. To invert the expression (3.25), i.e., to derive the elastic compliance tensor $\mathcal{M}_e = \mathcal{L}_e^{-1}$, it is convenient to change the basis \mathbf{I}^i into \mathbf{J}^i ($i = 1, 2, \dots, 6$) through the linear transformation:

$$\begin{aligned} \mathbf{J}^1 &= \frac{1}{2}(\mathbf{I}^2 - \mathbf{I}^3 - \mathbf{I}^4 + 3\mathbf{I}^6) , & \mathbf{J}^2 &= \frac{1}{2}(-\mathbf{I}^2 + \mathbf{I}^3 + \mathbf{I}^4 + \mathbf{I}^6) \\ \mathbf{J}^3 &= \frac{1}{2}(-2\mathbf{I}^3 - \mathbf{I}^4 + 3\mathbf{I}^6) , & \mathbf{J}^4 &= \frac{1}{2}(-2\mathbf{I}^3 + \mathbf{I}^4 + \mathbf{I}^6) \\ \mathbf{J}^5 &= 2(\mathbf{I}^5 - \mathbf{I}^6) , & \mathbf{J}^6 &= \frac{1}{2}(2\mathbf{I}^1 - \mathbf{I}^2 + \mathbf{I}^3 + \mathbf{I}^4 - 4\mathbf{I}^5 + \mathbf{I}^6) . \end{aligned} \quad (3.27)$$

The elastic stiffness (3.25) then becomes

$$\mathcal{L}_e = \sum_{i=1}^6 b_i \mathbf{J}^i . \quad (3.28)$$

The new parameters b_i in (3.28) are related to the parameters a_i in (3.26) by:

$$\begin{aligned} b_1 &= \frac{1}{2}(2a_1 + 3a_2 + 2a_3 + a_5 + a_6) , & b_2 &= \frac{1}{2}(-a_2 + 2a_3 + a_5 + a_6) \\ b_3 &= -\frac{3}{2}(a_2 + a_3) , & b_4 &= \frac{1}{2}(a_2 + a_3) \\ b_5 &= \frac{1}{2}(2a_1 + a_5) , & b_6 &= a_1 . \end{aligned} \quad (3.29)$$

The inverse of the fourth-order tensor (3.28) is (Kunin, 1983)

$$\mathcal{M}_e = \mathcal{L}_e^{-1} = \sum_{i=1}^6 c_i \mathbf{J}^i . \quad (3.30)$$

The scalar parameters c_i are related to parameters b_i , defined in (3.29), by

$$\{c_1, \dots, c_6\} = \left\{ \frac{b_1}{\Delta}, -\frac{b_2}{\Delta}, -\frac{b_3}{\Delta}, -\frac{b_4}{\Delta}, \frac{1}{b_5}, \frac{1}{b_6} \right\} , \quad (3.31)$$

where $\Delta = b_1^2 - b_2^2 - b_3^2 + b_4^2$.

Returning to the basis \mathbf{I}^i , the elastic compliance (3.30) becomes

$$\mathcal{M}_e = \sum_{i=1}^6 d_i \mathbf{I}^i , \quad (3.32)$$

where the coefficients d_i are:

$$\begin{aligned} d_1 &= c_6 , & d_2 &= \frac{1}{2}(c_1 - c_2 - c_6) \\ d_3 &= \frac{1}{2}(-c_1 + c_2 - 2c_3 - 2c_4 + c_6) , & d_4 &= \frac{1}{2}(-c_1 + c_2 - c_3 + c_4 + c_6) \\ d_5 &= 2(c_5 - c_6) , & d_6 &= \frac{1}{2}(3c_1 + c_2 + 3c_3 + c_4 - 4c_5 + c_6) . \end{aligned} \quad (3.33)$$

In the explicit component form, (3.32) reads

$$\begin{aligned} \mathcal{M}_{ijkl}^e &= d_1 \frac{1}{2}(\delta_{ik}\delta_{jl} + \delta_{il}\delta_{jk}) + d_2 \delta_{ij}\delta_{kl} \\ &\quad + d_3(\delta_{ij}n_k n_l + n_i n_j \delta_{kl}) \\ &\quad + d_5 \frac{1}{4}(\delta_{ik}n_j n_l + n_i n_k \delta_{jl} + \delta_{il}n_j n_k + n_i n_l \delta_{jk}) \\ &\quad + d_6 n_i n_j n_k n_l . \end{aligned} \quad (3.34)$$

In view of (3.29) and (3.31), $c_4 - c_3 = -2(c_3 + c_4)$; hence, from (3.33), $d_3 = d_4$. Thus, \mathcal{M}_e satisfies the reciprocity relation $\mathcal{M}_{ijkl} = \mathcal{M}_{klij}$, as well as the symmetry properties $\mathcal{M}_{ijkl} = \mathcal{M}_{jikl} = \mathcal{M}_{ijlk}$, imposed by the symmetry of the stress and strain tensors. The tensor (3.32), or (3.34), is the compliance tensor of the considered transversely isotropic material. The relationships between the parameters d_i and the elastic properties of the transversely isotropic material are easy to establish, and will be derived later in the report (Section 4.3).

3.5. APPLICATIONS

3.5.1. Uniaxial Loading

Consider first a prismatic specimen subjected to uniaxial (tensile or compressive) stress σ directed along the axis of rotational symmetry (Fig. 3.6). In this case $\sigma_{ij} = \sigma n_i n_j$, where $n_i = \delta_{i3}$. The corresponding strain is $E_{ij} = [(1 + \nu)n_i n_j - \nu \delta_{ij}] \epsilon$, where ν ($= \nu_{13} = \nu_{23}$) is the Poisson's coefficient in the (1,2) plane of elastic symmetry, while σ and ϵ are the longitudinal stress and strain. Application of (3.22) provides in this case the following stress-strain relationship

$$\sigma_{ij} = (A n_i n_j + B \delta_{ij}) \epsilon. \quad (3.35)$$

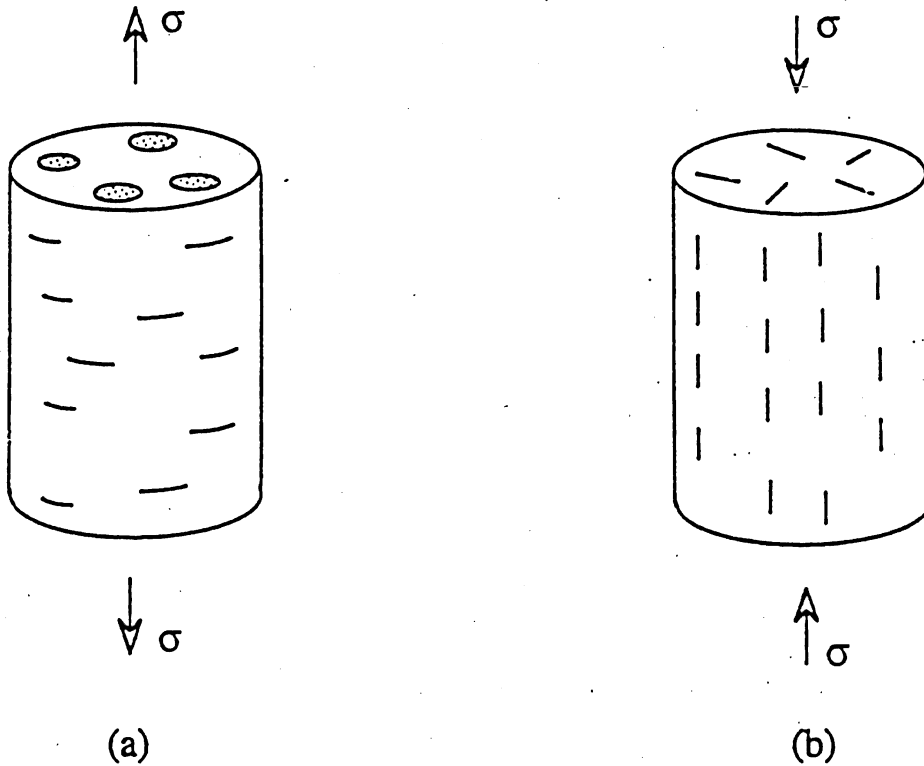


Figure 3.6. (a) Planar distribution of cracks: all cracks have their normals parallel to the longitudinal direction; (b) Cylindrical distribution of cracks: all cracks have their normals orthogonal to the longitudinal direction.

The parameters

$$A = (1 - \rho_n)[2\mu_0(1 - \rho_n) - \lambda_0 \Delta\rho] + 2\nu(1 - \rho_m)[\mu_0(1 - \rho_m) + \lambda_0 \Delta\rho] \quad (3.36)$$

and

$$B = (1 - \rho_m)[\lambda_0(1 - \rho_n) - 2\nu(\lambda_0 + \mu_0)(1 - \rho_m)] \quad (3.37)$$

serve as the repositories of the accumulated damage. Equating (3.35) with $\sigma_{ij} = \sigma n_i n_j$, it follows that $B = 0$ and $A\epsilon = \sigma$. The condition $B = 0$ provides the expression for the Poisson's coefficient

$$\nu = \frac{1 - \rho_n}{1 - \rho_m} \nu_0, \quad (3.38)$$

where $\nu_0 = \lambda_0/2(\lambda_0 + \mu_0)$ is the Poisson's coefficient of the undamaged isotropic material.

Expression (3.38) requires further explanation. If $\rho_m = 0$, (3.38) gives $\nu = (1 - \rho_n)\nu_0$, which is the value of the Poisson's coefficient of the transversely isotropic material containing cracks embedded in parallel planes normal to the longitudinal axis (Fig. 3.6a), and loaded in tension. The axial compression does not activate the cracks in Fig. 3.6a, and material behaves in compression as though it was undamaged ($\nu = \nu_0$).

If $\rho_n = 0$, (3.38) gives $\nu = (1 - \rho_m)^{-1}\nu_0$, which is the Poisson's coefficient of the transversely isotropic material with a cylindrical distribution of cracks (Fig. 3.6b), loaded in compression. This crack distribution is activated only in the presence of a compressive longitudinal stress, while it remains inactive when subjected to a longitudinal tensile stress.

From the remaining condition, $A\epsilon = \sigma$, it follows that the longitudinal Young's modulus is $\sigma/\epsilon = A$. In view of (3.38) and identity $\lambda_0 = 2\nu_0(\mu_0 + \lambda_0)$, (3.36) reduces to

$$A = (1 - \rho_n)^2 E_0, \quad (3.39)$$

where $E_0 = 2\mu_0(1 + \nu_0)$ is the Young's modulus of the undamaged isotropic matrix. When $\rho_n = 0$, the longitudinal Young's modulus becomes $A = E_0$ regardless of the existence of longitudinal cracks, i.e., whether ρ_m is equal to zero or not. If $\rho_n = 0$, the volumetric strain during the compression test is

$$E_{kk} = \frac{1}{E_0} \left(1 - \frac{2\nu_0}{1 - \rho_m}\right) \sigma, \quad (3.40)$$

or, by introducing the initial bulk modulus $\kappa_0 = E_0/3(1 - 2\nu_0)$,

$$E_{kk} = \frac{1}{3\kappa_0} \left(1 - \frac{2\nu_0}{1 - 2\nu_0} \frac{\rho_m}{1 - \rho_m} \right) \sigma. \quad (3.41)$$

During a gradual increase of compression σ (above some threshold value), ρ_m increases correspondingly. In the case when an appropriate damage law $\rho_m = \rho_m(\sigma)$ is additionally provided (from experimental evidence or by micromechanical considerations), (3.40) completely specifies the volumetric strain-stress response. A qualitative stress-strain dependence, depicted in Fig. 3.7a, replicates the basic features of experimentally observed behavior during an unconfined compression test ($\sigma < 0$) (see, for example, Jaeger and Cook, 1976). Volumetric strain is reduced to zero at deformation states for which the crack density is $\rho_m = 1 - 2\nu_0$.

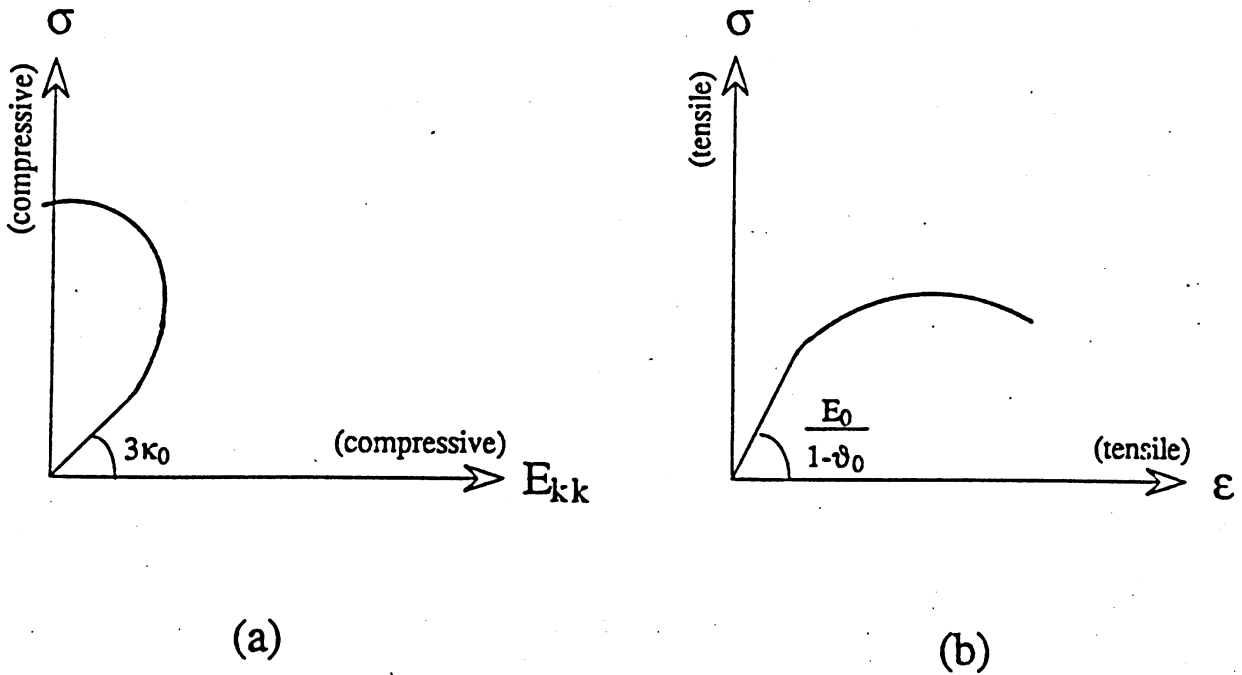


Figure 3.7. (a) Volumetric stress-strain response corresponding to eqn (3.41) of text: σ is the compressive stress, and E_{kk} is the corresponding volumetric strain, κ_0 is the undamaged bulk modulus; (b) Stress-strain response corresponding to eqn (3.49) of text: σ is the magnitude of the biaxial tension, and ϵ is the corresponding strain, E_0 and ν_0 are the undamaged Young's modulus and Poisson's ratio.

3.5.2. Biaxial Loading

Consider next the biaxial tensile loading $\sigma_{11} = \sigma_{22} = \sigma$ in the (1,2) plane of elastic symmetry. The corresponding stress and strain tensors are:

$$\begin{aligned}\sigma_{ij} &= (\delta_{ij} - n_i n_j) \sigma \\ E_{ij} &= [\delta_{ij} - (1 + \hat{\nu}) n_i n_j] \epsilon ,\end{aligned}\tag{3.42}$$

where ϵ is the magnitude of strain in the (1,2) plane, while $\hat{\nu} = 2\nu_{31}/(1 - \nu_{12})$ is the corresponding (effective) Poisson's coefficient. From (3.22) it further follows that

$$\sigma_{ij} = (C n_i n_j + D \delta_{ij}) \epsilon ,\tag{3.43}$$

in which the accumulated damage is recorded using the parameters

$$C = -2(1 - \rho_m)[\mu_0 (1 - \rho_m) + \lambda_0 \Delta \rho] - \hat{\nu}(1 - \rho_n)[2\mu_0 (1 - \rho_n) - \lambda_0 \Delta \rho] \tag{3.44}$$

and

$$D = (1 - \rho_m)[2(\lambda_0 + \mu_0) (1 - \rho_m) - \hat{\nu} \lambda_0 (1 - \rho_n)] .\tag{3.45}$$

Equating the first of equations (3.42) with (3.43) it follows that $D = -C$, and therefore

$$\hat{\nu} = \frac{1 - \rho_m}{1 - \rho_n} \hat{\nu}_0 ,\tag{3.46}$$

where $\hat{\nu}_0 = 2\lambda_0/(\lambda_0 + 2\mu_0) = 2\nu_0/(1 - \nu_0)$ is the effective Poisson's coefficient of the undamaged material. Substitution of (3.46) into (3.45) then gives

$$D = (1 - \rho_m)^2 \frac{E_0}{1 - \nu_0} .\tag{3.47}$$

The stress-strain equation (3.43), therefore, becomes

$$\sigma_{ij} = (1 - \rho_m)^2 \frac{E_0}{1 - \nu_0} (\delta_{ij} - n_i n_j) \epsilon .\tag{3.48}$$

The (σ, ϵ) relation can now be derived from (3.48) in conjunction with (3.42), as

$$\sigma = (1 - \rho_m)^2 \frac{E_0}{1 - \nu_0} \epsilon .\tag{3.49}$$

The (σ, ϵ) response is completely specified by (3.49) and the appropriate damage law $\rho_m = \rho_m(\sigma)$. A qualitative stress-strain dependence is depicted in Fig. 3.7b.

4.0 MICROMECHANICALLY INSPIRED DAMAGE MODELS FOR BRITTLE DEFORMATION OF ROCKS

4.1. ELASTIC BODY CONTAINING A PENNY-SHAPED CRACK

Expressions for the elastic stiffness and compliance can also be derived on the basis of micromechanical models. Consider a single penny-shaped crack embedded in an infinite isotropic elastic solid, uniformly loaded at infinity. We decompose this problem, as usual, into two problems: that of the body without a crack, loaded at infinity (⁰), and that of the body with a crack appropriately loaded over the crack faces (*). Correspondingly, the local strain e can be written as the sum of the strains belonging to two problems, i.e. $e = e^0 + e^*$. The averaged strains ($\epsilon = \frac{1}{V} \int_V e \, dV$ as $V \rightarrow \infty$) are decomposed in the same manner, $\epsilon = \epsilon^0 + \epsilon^*$. Let σ be the remote loading and \mathcal{M}_e^0 the elastic compliance of the virgin material without the crack. Introducing \mathcal{M}_e as the average elastic compliance of the body with a crack, and denoting by \mathcal{M}^* the compliance mapping σ to ϵ^* , $\epsilon^* = \mathcal{M}^* : \sigma$, it follows that

$$\mathcal{M}_e = \mathcal{M}_e^0 + \mathcal{M}^* . \quad (4.1)$$

The compliance \mathcal{M}^* , being the Hessian of the complementary strain energy $\Psi^* = \frac{1}{2} \mathcal{M}^* : (\sigma \otimes \sigma)$,

$$\mathcal{M}^* = \frac{\partial^2 \Psi^*}{\partial \sigma \otimes \partial \sigma} , \quad (4.2)$$

can be conveniently determined by observing that Ψ^* is equal to the energy release associated with the self-similar crack growth from zero to the current size a . As shown by Budiansky and Rice (1973), this energy can be expressed as

$$\Psi^* = \int_0^a \frac{M}{a} \, da , \quad (4.3)$$

where M is the M-conservation integral of fracture mechanics. The M integral can be written in terms of the J integral by means of a line integral along the crack edge l

$$M = \oint_l a J \, dl . \quad (4.4)$$

Substituting (4.4) into (4.3), it follows that

$$\Psi^* = \int_0^a \left(\oint_l J \, dl \right) da . \quad (4.5)$$

In the close neighborhood of the crack edge, the stress and strain states are a combination of plane strain and antiplane shear. Thus, the energy release rate or the J integral can be expressed in terms of the corresponding stress-intensity factors K_J ($J = I, II, III$) as

$$J = \frac{1 - \nu_0}{2\mu_0} (K_I^2 + K_{II}^2) + \frac{1}{2\mu_0} K_{III}^2 . \quad (4.6)$$

The expression (4.6) can be conveniently rewritten as (Sumarac, 1987)

$$J = C_{IJ} K_I K_J , \quad (4.7)$$

where

$$C_{IJ} = \frac{1}{2\mu_0} [(1 - \nu_0)\delta_{IJ} + \nu_0\delta_{III,I}\delta_{III,J}] .$$

Consequently, substituting (4.7) into (4.5) gives

$$\Psi^* = \int_0^a \left(\oint_l C_{IJ} K_I K_J dl \right) da . \quad (4.8)$$

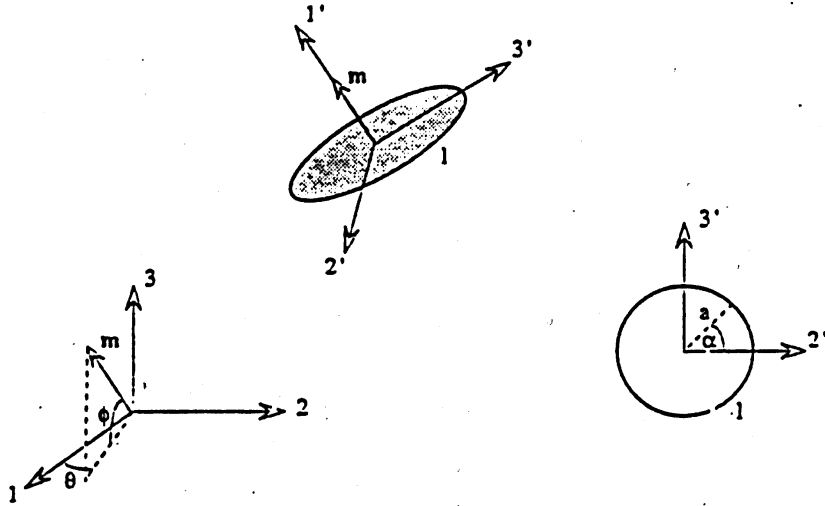


Figure 4.1. Penny-shaped crack of radius a and circumference l : $(1', 2', 3')$ denotes local crack coordinate system, direction $1'$ being coincident with normal to crack plane m ; angles θ and ϕ define orientation of vector m relative to global coordinate system $(1, 2, 3)$.

For a penny-shaped crack the stress-intensity factors, written in the symmetricized form, are (Tada, *et al.*, 1985):

$$K_I = \frac{2}{\pi}(\pi a)^{1/2} \sigma'_{11}$$

$$K_{II} = \frac{2}{\pi}(\pi a)^{1/2} \frac{1}{2 - \nu_0} [(\sigma'_{12} + \sigma'_{21})\cos\alpha + (\sigma'_{13} + \sigma'_{31})\sin\alpha] \quad (4.9)$$

$$K_{III} = \frac{2}{\pi}(\pi a)^{1/2} \frac{1 - \nu_0}{2 - \nu_0} [(\sigma'_{12} + \sigma'_{21})\sin\alpha - (\sigma'_{13} + \sigma'_{31})\cos\alpha],$$

where σ'_{ij} are the stress components in the crack coordinate system, and α is an angle defined in Fig. 4.1. The stress component σ'_{11} is assumed to be tensile. Differentiating (4.9) it follows that:

$$\frac{\partial K_I}{\partial \sigma'_{ij}} = \frac{2}{\pi}(\pi a)^{1/2} \delta_{i1} \delta_{j1}$$

$$\frac{\partial K_{II}}{\partial \sigma'_{ij}} = \frac{2}{\pi}(\pi a)^{1/2} \frac{1}{2 - \nu_0} [(\delta_{i1} \delta_{j2} + \delta_{i2} \delta_{j1})\cos\alpha + (\delta_{i1} \delta_{j3} + \delta_{i3} \delta_{j1})\sin\alpha] \quad (4.10)$$

$$\frac{\partial K_{III}}{\partial \sigma'_{ij}} = \frac{2}{\pi}(\pi a)^{1/2} \frac{1 - \nu_0}{2 - \nu_0} [(\delta_{i1} \delta_{j2} + \delta_{i2} \delta_{j1})\sin\alpha - (\delta_{i1} \delta_{j3} + \delta_{i3} \delta_{j1})\cos\alpha].$$

If σ'_{11} is a compressive stress, $K_I = 0$ along with the right-hand side of the first expression in (4.10).

The components of the compliance tensor \mathcal{M}^* in the local (crack) coordinate system are

$$\mathcal{M}_{ijkl}^* = \frac{\partial^2 \Psi^*}{\partial \sigma'_{ij} \partial \sigma'_{kl}} = 2 \int_0^a \left(\oint_I C_{IJ} \frac{\partial K_I}{\partial \sigma'_{ij}} \frac{\partial K_J}{\partial \sigma'_{kl}} dl \right) da. \quad (4.11)$$

Since

$$C_{IJ} \frac{\partial K_I}{\partial \sigma'_{ij}} \frac{\partial K_J}{\partial \sigma'_{kl}} = \frac{1 - \nu_0}{2\mu_0} \left(\frac{\partial K_I}{\partial \sigma'_{ij}} \frac{\partial K_I}{\partial \sigma'_{kl}} + \frac{\partial K_{II}}{\partial \sigma'_{ij}} \frac{\partial K_{II}}{\partial \sigma'_{kl}} \right) + \frac{1}{2\mu_0} \frac{\partial K_{III}}{\partial \sigma'_{ij}} \frac{\partial K_{III}}{\partial \sigma'_{kl}}, \quad (4.12)$$

substitution of (4.10) and (4.12) into (4.11) leads to the following expression for the compliance tensor

$$\mathcal{M}_{ijkl}^* = \frac{16}{3} \frac{1-\nu_0}{2\mu_0} a^3 \{ (\delta_{i1}\delta_{j1}\delta_{k1}\delta_{l1}) H(\sigma'_{11}) + \frac{1}{2(2-\nu_0)} [(\delta_{i1}\delta_{j2} + \delta_{i2}\delta_{j1})(\delta_{k1}\delta_{l2} + \delta_{k2}\delta_{l1}) + (\delta_{i1}\delta_{j3} + \delta_{i3}\delta_{j1})(\delta_{k1}\delta_{l3} + \delta_{k3}\delta_{l1})] \} . \quad (4.13)$$

The Heaviside step function $H(\sigma'_{11})$ is introduced in (4.13) to simultaneously treat the possibility of tensile and compressive stress components σ'_{11} . In the local crack coordinate system, the normal to the crack plane has the components

$$m'_i = \delta_{i1} . \quad (4.14)$$

The expression for the compliance tensor (4.13) thus becomes

$$\begin{aligned} \mathcal{M}_{ijkl}^* &= \frac{16}{3} \frac{1-\nu_0}{2\mu_0} a^3 \{ (m'_i m'_j m'_k m'_l) H(\sigma'_{11}) \\ &\quad + \frac{1}{2(2-\nu_0)} [(m'_i \delta_{j2} + \delta_{i2} m'_j)(m'_k \delta_{l2} + \delta_{k2} m'_l) + (m'_i \delta_{j3} + \delta_{i3} m'_j)(m'_k \delta_{l3} + \delta_{k3} m'_l)] \} . \end{aligned} \quad (4.15)$$

The expression (4.15) can be further rearranged as

$$\begin{aligned} \mathcal{M}_{ijkl}^* &= \frac{16}{3} \frac{1-\nu_0}{2\mu_0} a^3 [(m'_i m'_j m'_k m'_l) H(\sigma'_{11}) \\ &\quad + \frac{1}{2(2-\nu_0)} (\delta_{ik} m'_j m'_l + m'_i m'_k \delta_{jl} + \delta_{il} m'_j m'_k + m'_i m'_l \delta_{jk} - 4 m'_i m'_j m'_k m'_l)] . \end{aligned} \quad (4.16)$$

The required symmetry properties $\mathcal{M}_{ijkl}^* = \mathcal{M}_{jikl}^* = \mathcal{M}_{ijlk}^* = \mathcal{M}_{klij}^*$ clearly hold. Using the fourth-order tensors forming the integrity basis I^i , introduced in Section 3.3, expression (4.16) can be rewritten in compact form as

$$\mathcal{M}_{ijkl}^* = \frac{16}{3} \frac{1-\nu_0}{2-\nu_0} \frac{1}{2\mu_0} a^3 \{ 2 I_{ijkl}^{5, m'} + [(2-\nu_0)H(\sigma'_{11}) - 2] I_{ijkl}^{6, m'} \} . \quad (4.17)$$

In (4.17), $I_{ijkl}^{5, m'}$ and $I_{ijkl}^{6, m'}$ are the tensors defined by (3.17), in terms of the components of the normal m relative to the local crack coordinate system ($m'_i = \delta_{i1}$). If $\sigma'_{11} \geq 0$, (4.17) further reduces to

$$\mathcal{M}_{ijkl}^* = \frac{16}{3} \frac{1-\nu_0}{2-\nu_0} \frac{1}{2\mu_0} a^3 (2 I_{ijkl}^{5, m'} - \nu_0 I_{ijkl}^{6, m'}) , \quad (4.18)$$

used by Krajcinovic and Fanella (1986).

4.2. AVERAGING PROCEDURE

The compliance tensor expressed in (4.17) relative to the local crack coordinate system, can be written in the global coordinate system using the coordinate transformation

$$\mathcal{M}_{ijkl}^* = Q_{i\alpha} Q_{j\beta} \mathcal{M}_{\alpha\beta\gamma\delta}^* Q_{k\gamma} Q_{l\delta} ,$$

where \mathbf{Q} is the orthogonal tensor of the transformation between the two coordinate systems. Substitution of (4.17) gives

$$\mathcal{M}_{ijkl}^* = \frac{16}{3} \frac{1-\nu_0}{2-\nu_0} \frac{1}{2\mu_0} a^3 \{ 2 I_{ijkl}^{5,m} + [(2-\nu_0)H(\mathbf{m}^T \cdot \boldsymbol{\sigma} \cdot \mathbf{m}) - 2] I_{ijkl}^{6,m} \} , \quad (4.19)$$

where:

$$\begin{aligned} I_{ijkl}^{5,m} &= \frac{1}{4} (\delta_{ik} m_j m_l + m_i m_k \delta_{jl} + \delta_{il} m_j m_k + m_i m_l \delta_{jk}) \\ I_{ijkl}^{6,m} &= m_i m_j m_k m_l \end{aligned} \quad (4.20)$$

are the fourth-order tensors combining the Kronecker delta and the unit vector \mathbf{m} , which is expressed in the global coordinate system as

$$\mathbf{m} = \{ \cos\phi \cos\theta , \cos\phi \sin\theta , \sin\phi \} .$$

If $\sigma'_{11} = \mathbf{m}^T \cdot \boldsymbol{\sigma} \cdot \mathbf{m} \geq 0$ ($\boldsymbol{\sigma}$ is the stress tensor with components in the global coordinate system), (4.19) reduces to

$$\mathcal{M}_{ijkl}^* = \frac{16}{3} \frac{1-\nu_0}{2-\nu_0} \frac{1}{2\mu_0} a^3 (2 I_{ijkl}^{5,m} - \nu_0 I_{ijkl}^{6,m}) . \quad (4.21)$$

Expressions (4.21) and (4.18) are equal, except that in (4.18) the components of the normal \mathbf{m} are expressed in the local crack coordinate system, while in (4.21) they are expressed relative to the global coordinate system. The superscript m indicates that the reference is to the plane of the crack (Fig. 4.1).

Consider now the case of many cracks. If all cracks have the same normal \mathbf{m} , the average compliance (neglecting the direct crack interaction) is $\bar{\mathcal{M}}^* = N \mathcal{M}^*$, where N is the number of cracks per unit volume. Next, let the crack distribution be such that all normals to the crack planes have the same angle $\phi = \text{constant}$. Neglecting direct interaction between adjacent cracks (dilute distribution of cracks), the average compliance is

$$\begin{aligned}\bar{\mathcal{M}}_{ijkl}^* &= \frac{N}{2\pi} \int_0^{2\pi} \mathcal{M}_{ijkl}^* d\theta = \\ &= \frac{N}{2\pi} \frac{16}{3} \frac{1-\nu_0}{2-\nu_0} \frac{1}{2\mu_0} a^3 \left(2 \int_0^{2\pi} I_{ijkl}^{5,m} d\theta - \nu_0 \int_0^{2\pi} I_{ijkl}^{6,m} d\theta \right).\end{aligned}\quad (4.22)$$

In (4.22) the stress state is assumed to be such that $\mathbf{m}^T \cdot \boldsymbol{\sigma} \cdot \mathbf{m} \geq 0$ for all \mathbf{m} , allowing substitution of (4.21) for the components of the compliance tensor \mathcal{M}_{ijkl}^* .

In general, for an arbitrary angle ϕ

$$\begin{aligned}m_i m_j &= \delta_{i1} \delta_{j1} \cos^2 \phi \cos^2 \theta + \delta_{i2} \delta_{j2} \cos^2 \phi \sin^2 \theta + \delta_{i3} \delta_{j3} \sin^2 \phi \\ &+ (\delta_{i1} \delta_{j2} + \delta_{i2} \delta_{j1}) \cos^2 \phi \sin \theta \cos \theta + (\delta_{i1} \delta_{j3} + \delta_{i3} \delta_{j1}) \sin \phi \cos \phi \cos \theta \\ &+ (\delta_{i2} \delta_{j3} + \delta_{i3} \delta_{j2}) \sin \phi \cos \phi \sin \theta.\end{aligned}\quad (4.23)$$

Consider first an important special case for which $\phi = 0$. The normal \mathbf{m} has components $\{\cos \theta, \sin \theta, 0\}$. In this case (4.23) reduces to

$$m_i m_j = \delta_{i1} \delta_{j1} \cos^2 \theta + \delta_{i2} \delta_{j2} \sin^2 \theta + (\delta_{i1} \delta_{j2} + \delta_{i2} \delta_{j1}) \sin \theta \cos \theta. \quad (4.24)$$

Hence

$$\int_0^{2\pi} m_i m_j d\theta = \pi(\delta_{i1} \delta_{j1} + \delta_{i2} \delta_{j2}) = \pi(\delta_{ij} - \delta_{i3} \delta_{j3}). \quad (4.25)$$

Introduce the vector \mathbf{n} , normal to \mathbf{m} , having the components

$$n_i = \delta_{i3} \quad (4.26)$$

in the global coordinate system. The integral (4.25) can be accordingly written as

$$\int_0^{2\pi} m_i m_j d\theta = \pi(\delta_{ij} - n_i n_j), \quad (4.27)$$

such that

$$\begin{aligned}\int_0^{2\pi} I_{ijkl}^{5,m} d\theta &= \frac{\pi}{4} [2(\delta_{ik} \delta_{jl} + \delta_{il} \delta_{jk}) \\ &- (\delta_{ik} n_j n_l + n_i n_k \delta_{jl} + \delta_{il} n_j n_k + n_i n_l \delta_{jk})].\end{aligned}\quad (4.28)$$

Using the fourth-order tensors of the integrity basis \mathbf{I}^i introduced in (3.17), the integral (4.28) can be rewritten in compact form as

$$\int_0^{2\pi} I^{5m} d\theta = \pi(I^1 - I^{5n}) . \quad (4.29)$$

To evaluate the integral

$$\int_0^{2\pi} I_{ijkl}^{6m} d\theta = \int_0^{2\pi} m_i m_j m_k m_l d\theta , \quad (4.30)$$

expressions of the type (4.24) are substituted for products $m_i m_j$ and $m_k m_l$. Performing the intergration, one obtains

$$\begin{aligned} \int_0^{2\pi} I_{ijkl}^{6m} d\theta = \frac{\pi}{4} [& 3(\delta_{i1}\delta_{j1}\delta_{k1}\delta_{l1} + \delta_{i2}\delta_{j2}\delta_{k2}\delta_{l2}) \\ & + (\delta_{i1}\delta_{j2}\delta_{k1}\delta_{l2} + \delta_{i1}\delta_{j2}\delta_{k2}\delta_{l1} + \delta_{i2}\delta_{j1}\delta_{k1}\delta_{l2} \\ & + \delta_{i2}\delta_{j1}\delta_{k2}\delta_{l1} + \delta_{i1}\delta_{j1}\delta_{k2}\delta_{l2} + \delta_{i2}\delta_{j2}\delta_{k1}\delta_{l1})] . \end{aligned} \quad (4.31)$$

After a somewhat delicate rearrangement of terms, (4.31) can be cast in the following remarkably simple form

$$\begin{aligned} \int_0^{2\pi} I_{ijkl}^{6m} d\theta = \frac{\pi}{4} [& (\delta_{ij} - n_i n_j)(\delta_{kl} - n_k n_l) \\ & + (\delta_{jk} - n_j n_k)(\delta_{il} - n_i n_l) + (\delta_{ki} - n_k n_i)(\delta_{jl} - n_j n_l)] , \end{aligned} \quad (4.32)$$

or

$$\begin{aligned} \int_0^{2\pi} I_{ijkl}^{6m} d\theta = \frac{\pi}{4} [& (\delta_{ik}\delta_{jl} + \delta_{il}\delta_{jk}) + \delta_{ij}\delta_{kl} - (\delta_{ij}n_k n_l + n_i n_j \delta_{kl}) \\ & - (\delta_{ik}n_j n_l + n_i n_k \delta_{jl} + \delta_{il}n_j n_k + n_i n_l \delta_{jk}) + 3(n_i n_j n_k n_l)] . \end{aligned} \quad (4.33)$$

Utilizing the fourth-order tensors forming the integrity basis (3.17), (4.33) can be written as

$$\int_0^{2\pi} I^{6m} d\theta = \frac{\pi}{4} (2 I^1 + I^2 - I^{3n} - I^{4n} - 4 I^{5n} + 3 I^{6n}) . \quad (4.34)$$

Finally, the average compliance due to the considered crack distribution is derived by substituting (4.28) and (4.33) into (4.22)

$$\begin{aligned} \bar{\mathcal{M}}_{ijkl}^* = \frac{2}{3} \frac{1 - \nu_0}{2 - \nu_0} \frac{1}{2\mu_0} \omega [& (4 - \nu_0) (\delta_{ik}\delta_{jl} + \delta_{il}\delta_{jk}) - \nu_0 \delta_{ij}\delta_{kl} + \nu_0 (\delta_{ij}n_k n_l + n_i n_j \delta_{kl}) \\ & - (2 - \nu_0) (\delta_{ik}n_j n_l + n_i n_k \delta_{jl} + \delta_{il}n_j n_k + n_i n_l \delta_{jk}) - 3\nu_0 (n_i n_j n_k n_l)] . \end{aligned} \quad (4.35)$$

The nondimensional scalar quantity $\omega = Na^3$, originally introduced by Budiansky and O'Connell (1976), represents a micromechanical damage parameter (measure) defining the density of the considered crack distribution within the representative volume element. Note that $\bar{\mathcal{M}}^*$ is linearly proportional to ω , i.e. $\bar{\mathcal{M}}^* = \omega \mathcal{M}^*$, where \mathcal{M}^* is the constant tensor given by

$$\mathcal{M}^* = \frac{2}{3} \frac{1 - \nu_0}{2 - \nu_0} \frac{1}{2\mu_0} [2(4 - \nu_0) \mathbf{I}^1 - \nu_0 \mathbf{I}^2 + \nu_0 (\mathbf{I}^{3n} + \mathbf{I}^{4n}) - 4(2 - \nu_0) \mathbf{I}^{5n} - 3\nu_0 \mathbf{I}^{6n}] .$$

Finally, if the crack distribution is dilute and isotropic, the average compliance is

$$\bar{\mathcal{M}}^* = \frac{N}{4\pi} \int_0^{2\pi} \int_{-\pi/2}^{\pi/2} \mathcal{M}^* \cos\phi \, d\phi \, d\theta . \quad (4.36)$$

By using (4.20) and (4.23) it can be shown that:

$$\begin{aligned} \int_0^{2\pi} \int_{-\pi/2}^{\pi/2} \mathbf{I}^{5m} \cos\phi \, d\phi \, d\theta &= \frac{4\pi}{3} \mathbf{I}^1 \\ \int_0^{2\pi} \int_{-\pi/2}^{\pi/2} \mathbf{I}^{6m} \cos\phi \, d\phi \, d\theta &= \frac{4\pi}{15} (2 \mathbf{I}^1 + \mathbf{I}^2) . \end{aligned} \quad (4.37)$$

The average compliance is derived by substituting (4.37) into (4.21) and (4.36)

$$\bar{\mathcal{M}}^* = \frac{16}{45} \frac{1 - \nu_0}{2 - \nu_0} \frac{1}{2\mu_0} \omega [2(5 - \nu_0) \mathbf{I}^1 - \nu_0 \mathbf{I}^2] . \quad (4.38)$$

It is easily shown that (4.38) produces the compliance components identical to those given by Equation (20) of Horii and Nemat-Nasser (1983).

4.3. EFFECTIVE COMPLIANCE TENSOR

The compliance tensor of the undamaged, isotropic and homogeneous elastic matrix is

$$\mathcal{M}_{ijkl}^0 = \frac{1}{2\mu_0} \left[\frac{1}{2} (\delta_{ik}\delta_{jl} + \delta_{il}\delta_{jk}) - \frac{\nu_0}{1 + \nu_0} \delta_{ij}\delta_{kl} \right] .$$

Using the basis \mathbf{I}^i introduced in Section 3.3, above can be rewritten as

$$\mathcal{M}_e^0 = \frac{1}{2\mu_0} \left(\mathbf{I}^1 - \frac{\nu_0}{1 + \nu_0} \mathbf{I}^2 \right) . \quad (4.39)$$

The overall (effective) compliance is derived by superposing (4.39) and the expression for the average compliance $\bar{\mathcal{M}}^*$. If the crack distribution is isotropic, i.e. if $\bar{\mathcal{M}}^*$ is defined by (4.38), the overall compliance becomes

$$\mathcal{M}_e^0 = \frac{1}{2\mu} \left(I^1 - \frac{\nu}{1+\nu} I^2 \right), \quad (4.40)$$

where the damage-dependent shear modulus and Poisson's ratio are given by:

$$\begin{aligned} \mu &= \frac{45(2-\nu_0)}{45(2-\nu_0) + 32(1-\nu_0)(5-\nu_0)\omega} \mu_0 \\ \nu &= \frac{45(2-\nu_0) + 16(1-\nu_0^2)\omega}{45(2-\nu_0) + 16(1-\nu_0^2)(10-3\nu_0)\omega} \nu_0. \end{aligned} \quad (4.41)$$

If the crack distribution is of the type shown in Fig. 3.6b, such that (4.35) applies, it follows that

$$\begin{aligned} \mathcal{M}_{ijkl}^e &= \frac{1}{2\mu_0} \left\{ \left[1 + \frac{4(4-\nu_0)(1-\nu_0)}{3(2-\nu_0)} \omega \right] \frac{1}{2} (\delta_{ik}\delta_{jl} + \delta_{il}\delta_{jk}) \right. \\ &\quad - \left[\frac{\nu_0}{1+\nu_0} + \frac{2\nu_0(1-\nu_0)}{3(2-\nu_0)} \omega \right] \delta_{ij}\delta_{kl} + \frac{2(1-\nu_0)}{3(2-\nu_0)} \omega [2(\delta_{ij}n_k n_l + n_i n_j \delta_{kl}) \\ &\quad \left. - (2-\nu_0)(\delta_{ik}n_j n_l + n_i n_k \delta_{jl} + \delta_{il}n_j n_k + n_i n_l \delta_{jk}) - 3\nu_0(n_i n_j n_k n_l)] \right\}. \end{aligned} \quad (4.42)$$

Expression (4.42) represents the compliance tensor of a transversely isotropic material whose plane of symmetry is normal to the direction \mathbf{n} . Indeed, (4.42) can be rewritten as

$$\mathcal{M}_e = \sum_{i=1}^6 C_i \mathbf{J}^i, \quad (4.43)$$

with the obvious expressions for the parameters C_i . In terms of the elastic moduli and Poisson's ratios in two orthogonal directions, the parameters C_i are:

$$\begin{aligned} C_1 &= \frac{1+\nu}{E} = \frac{1}{2\mu}, & C_2 &= -\frac{\nu}{E} \\ C_3 &= \frac{\nu}{E} - \frac{\nu'}{E'}, & C_4 &= \frac{\nu}{E} - \frac{\nu'}{E'} = C_3 \\ C_5 &= \frac{1}{\mu'} - \frac{1}{\mu}, & C_6 &= \frac{1+2\nu'}{E'} - \frac{\nu}{E} + \frac{1}{2\mu} - \frac{1}{\mu'}. \end{aligned} \quad (4.44)$$

Here, E is the Young's modulus in the plane of isotropy and E' is in the direction normal to it. Also, ν is the Poisson's ratio characterizing transverse contraction in the plane of isotropy when tension is applied in the same plane, while ν' is the Poisson's ratio obtained when tension is applied normal to the plane of isotropy. μ' is the shear modulus for any plane perpendicular to the plane of isotropy (Lekhnitskii, 1981). These five material parameters can be derived from (4.44) in terms of the parameters C_i as:

$$\begin{aligned}
E &= \frac{1}{C_1 + C_2}, & \nu &= -\frac{C_2}{C_1 + C_2}, \\
E' &= \frac{1}{C_1 + C_2 + 2C_3 + C_5 + C_6}, & \nu' &= -\frac{C_2 + C_3}{C_1 + C_2 + 2C_3 + C_5 + C_6}, \\
\mu' &= \frac{1}{2C_1 + C_5}.
\end{aligned} \tag{4.45}$$

4.4. EFFECTIVE STIFFNESS TENSOR

To derive the expression for the stiffness tensor, being the inverse of the compliance tensor (4.42) from Section 4.3, it is convenient to use the fourth-order tensors of the basis \mathbf{J}^i , defined by (3.27). In this basis, the tensor (4.35) takes the form

$$\bar{\mathcal{M}}^* = \frac{4}{3} \frac{1 - \nu_0}{2 - \nu_0} \frac{1}{2\mu_0} \omega [(2 - \nu_0) (\mathbf{J}^{1n} - \mathbf{J}^{2n}) + 2 \mathbf{J}^{5n} + (4 - \nu_0) \mathbf{J}^{6n}]. \tag{4.46}$$

Since:

$$\begin{aligned}
\mathbf{I}^1 &= \mathbf{J}^1 + \mathbf{J}^5 + \mathbf{J}^6 \\
\mathbf{I}^2 &= \frac{1}{2} (3 \mathbf{J}^1 - \mathbf{J}^2 - 3 \mathbf{J}^3 + \mathbf{J}^4),
\end{aligned}$$

the initial compliance \mathcal{M}_e^0 , given by (4.39), can be expressed in terms of the \mathbf{J}^i basis. The overall compliance $\mathcal{M}_e = \mathcal{M}_e^0 + \bar{\mathcal{M}}^*$, consequently becomes

$$\mathcal{M}_e = \frac{1}{2\mu_0} \sum_{i=1}^6 c_i \mathbf{J}^i, \tag{4.47}$$

where:

$$\begin{aligned}
c_1 &= \frac{2 - \nu_0}{2(1 + \nu_0)} + \frac{4}{3}(1 - \nu_0) \omega, & c_2 &= \frac{\nu_0}{2(1 + \nu_0)} - \frac{4}{3}(1 - \nu_0) \omega, \\
c_3 &= \frac{3\nu_0}{2(1 + \nu_0)}, & c_4 &= -\frac{\nu_0}{2(1 + \nu_0)}, \\
c_5 &= 1 + \frac{8(1 - \nu_0)}{3(2 - \nu_0)} \omega, & c_6 &= 1 + \frac{4(1 - \nu_0)(4 - \nu_0)}{3(2 - \nu_0)} \omega.
\end{aligned} \tag{4.48}$$

The tensor representation (4.47) has the explicit inverse

$$\mathcal{L}_e = \mathcal{M}_e^{-1} = 2\mu_0 \sum_{i=1}^6 b_i \mathbf{J}^i, \tag{4.49}$$

where

$$\{b_1, \dots, b_6\} = \left\{ \frac{c_1}{\Delta}, -\frac{c_2}{\Delta}, -\frac{c_3}{\Delta}, -\frac{c_4}{\Delta}, \frac{1}{c_5}, \frac{1}{c_6} \right\}, \quad (4.50)$$

and $\Delta = c_1^2 - c_2^2 - c_3^2 + c_4^2$. Using the transformation rule (3.27), (4.49) can be expressed in terms of the original I^i basis as

$$\mathcal{L}_e = 2\mu_0 \sum_{i=1}^6 a_i I^i. \quad (4.51)$$

The coefficients a_i are related to coefficients b_i by:

$$\begin{aligned} a_1 &= b_6, & a_2 &= \frac{1}{2}(b_1 - b_2 - b_6) \\ a_3 &= \frac{1}{2}(-b_1 + b_2 - 2b_3 - 2b_4 + b_6), & a_4 &= \frac{1}{2}(-b_1 + b_2 - b_3 + b_4 + b_6) \\ a_5 &= 2(b_5 - b_6), & a_6 &= \frac{1}{2}(3b_1 + b_2 + 3b_3 + b_4 - 4b_5 + b_6) \end{aligned} \quad (4.52)$$

which is identical to the relationship (3.33) existing between the coefficients d_i and c_i . In the component form, (4.51) reads

$$\begin{aligned} \mathcal{L}_{ijkl}^e &= 2\mu_0 \left[a_1 \frac{1}{2}(\delta_{ik}\delta_{jl} + \delta_{il}\delta_{jk}) + a_2 \delta_{ij}\delta_{kl} \right. \\ &\quad + a_3(\delta_{ij}n_k n_l + n_i n_j \delta_{kl}) \\ &\quad + a_5 \frac{1}{4}(\delta_{ik}n_j n_l + n_i n_k \delta_{jl} + \delta_{il}n_j n_k + n_i n_l \delta_{jk}) \\ &\quad \left. + a_6 n_i n_j n_k n_l \right]. \end{aligned} \quad (4.53)$$

Expression (4.53) is the exact inverse of (4.42). If the damage parameter ω is sufficiently small so that the quadratic and higher-order terms in ω can be neglected, coefficients of (4.53) simplify accordingly and become:

$$\begin{aligned} a_1 &= 1 - \frac{4}{3} \frac{(1 - \nu_0)(4 - \nu_0)}{2 - \nu_0} \omega \\ a_2 &= \frac{\nu_0}{1 - 2\nu_0} - \frac{2}{3} \frac{\nu_0(1 - \nu_0)}{(2 - \nu_0)(1 - 2\nu_0)^2} (15 - 20\nu_0 + 4\nu_0^2) \omega \\ a_3 &= a_4 = \frac{2}{3} \frac{\nu_0(1 - \nu_0)}{(2 - \nu_0)(1 - 2\nu_0)^2} (7 - 16\nu_0 + 4\nu_0^2) \omega \\ a_5 &= \frac{8}{3} (1 - \nu_0) \omega \end{aligned} \quad (4.54)$$

$$a_6 = -\frac{2}{3} \frac{\nu_0(1-\nu_0)}{(2-\nu_0)(1-2\nu_0)} (13-2\nu_0) \omega .$$

It is easy to prove that for this case the components of (4.53) are identical to the components of the stiffness tensor obtained by Nemat-Nasser and Hori (1990) (their Equation (5.11b)). Also, from (4.53) and (4.54) it clearly follows that $\mathcal{L}_e = \mathcal{L}_e^0 + \omega \mathbf{L}^*$, where

$$\mathbf{L}^* = \frac{2\mu_0}{\omega} \left[(a_1 - 1) \mathbf{I}^1 + \left(a_2 - \frac{\nu_0}{1-2\nu_0} \right) \mathbf{I}^2 + a_3 (\mathbf{I}^3 + \mathbf{I}^4) + a_5 \mathbf{I}^5 + a_6 \mathbf{I}^6 \right], \quad (4.55)$$

and $\mathcal{L}_e^0 = 2\mu_0(\mathbf{I}^1 + \frac{\nu_0}{1-2\nu_0} \mathbf{I}^2)$.

4.5. AXIAL COMPRESSION OF A Laterally Confined Specimen

Consider a cylindrical specimen subjected to an axial compression $\sigma + p$ and lateral confining pressure p . The stress difference (between axial and lateral stress), commonly used in rock mechanics, is σ . The state of macroscopic stress is therefore

$$\sigma_{ij} = -(p \delta_{ij} + \sigma n_i n_j), \quad (4.56)$$

where $n_i = \delta_{i3}$ is a unit vector collinear with the longitudinal axis of the cylinder. Even though the applied tractions are compressive, local tensile stresses may arise in the vicinity of the microstructural inhomogeneities (pores, pre-existing cracks, rigid inclusions, etc.). Introducing the influence tensor \mathcal{B} of the given microstructural inhomogeneity (Hill, 1967), one can write the local stress tensor as $\sigma^* = \mathcal{B} : \sigma$, where \mathcal{B} depends on the location and topology of the particular defect. At a low level of lateral confinement the local tensile stresses may suffice to nucleate new microcracks and propagate existing ones. The ensuing deformation is brittle, i.e., the inelastic deformation is directly related to the formation of new internal surfaces (nucleation of new cracks and growth of existing ones) in the specimen. Assuming that these microcracks develop in planes with normals perpendicular to the longitudinal (axial) direction \mathbf{n} (Fig. 3.6b), the initially isotropic material becomes transversely isotropic. In the simplest representation, the local tensile stress driving the microcrack growth (Fig. 4.2), can be written as

$$\sigma_{ij}^* = \sigma^* (\delta_{ij} - n_i n_j), \quad (4.57)$$

where the magnitude of the local tension σ^* depends on the microstructure, i.e., on the defects such as porosity or void distributions, and the stress difference σ . The influence tensor \mathcal{B} corresponding to the local stress given by the simplified representation (4.57) is not unique. One of its possible representations, satisfying $\sigma^* = \mathcal{B} : \sigma$, is $\mathcal{B} = \alpha [\mathbf{I}^1 - \frac{1}{2}(1 + \beta)(\mathbf{I}^2 - \mathbf{I}^3)]$, where $\alpha = \sigma^*/\sigma$ and $\beta = \sigma/p$.

The strain resulting from the crack openings due to the stress (4.57) is

$$\epsilon_{ij}^* = \bar{\mathcal{M}}_{ijkl}^* \sigma_{kl}^*, \quad (4.58)$$

where $\bar{\mathcal{M}}_{ijkl}^*$ is the compliance tensor, given by (4.35). Hence,

$$\epsilon_{ij}^* = \frac{8}{3}(1 - \nu_0) \omega \frac{\sigma^*}{2\mu_0} (\delta_{ij} - n_i n_j). \quad (4.59)$$

The strain due to macroscopic stress in the material without damage (i.e., with the initial, frozen microstructure) is

$$\epsilon_{ij}^0 = \mathcal{M}_{ijkl}^0 \sigma_{kl}, \quad (4.60)$$

i.e., in view of (4.56) and (4.39),

$$\epsilon_{ij}^0 = \frac{1}{2\mu_0} \left\{ \frac{1}{1 + \nu_0} [\nu_0 \sigma - (1 - 2\nu_0)p] \delta_{ij} - \sigma n_i n_j \right\}. \quad (4.61)$$

Defining the total strain as $\epsilon_{ij} = \epsilon_{ij}^* + \epsilon_{ij}^0$, it follows that the longitudinal strain is

$$\epsilon_{33} = -\frac{1}{E_0} [\sigma + (1 - 2\nu_0)p], \quad (4.62)$$

where $E_0 = 2\mu_0(1 + \nu_0)$ is the initial Young's modulus of the undamaged material. The total volumetric strain is

$$\epsilon_{kk} = \frac{1}{3\kappa_0} \left[\frac{16}{3} \frac{1 - \nu_0^2}{1 - 2\nu_0} \omega \sigma^* - (3p + \sigma) \right]. \quad (4.63)$$

In (4.63), $\kappa_0 = E_0/3(1 - 2\nu_0)$ is the bulk modulus of the undamaged matrix. Consequently, as a result of the introduced simplifications, the longitudinal strain (4.62) is not influenced by the damage. This is consistent with the assumption that the components of the crack-induced displacement discontinuities in the direction parallel to the specimen axis are zero. On the other hand, the non-zero strain components $\epsilon_{11}^* = \epsilon_{22}^*$ contribute to damage-affected volumetric strain, given by (4.63). With the additionally provided relationship defining the variation of the parameter $\omega \sigma^*$ as a function of increasing stress σ and pressure p , (4.63) suffices for the determination of the volumetric strain-stress response. The qualitative dependence is as shown in Fig. 3.7a.

If the specimen is not confined ($p = 0$), the Poisson's coefficient ν' in the (1,2) plane of elastic symmetry due to compression in the direction of the x_3 axis ($\nu' = -\epsilon_{11}/\epsilon_{33} = -\epsilon_{22}/\epsilon_{33} = \frac{1}{2}(1 - \epsilon_{kk}/\epsilon_{33})$) follows from (4.62) and (4.63)

$$\nu' = \nu_0 + \frac{8}{3}(1 - \nu_0^2)\omega \frac{\sigma^*}{\sigma} . \quad (4.64)$$

Again, if the relationship between $\omega\sigma^*$ and the applied stress is known, (4.64) specifies the change of the Poisson's ratio ν' caused by continuing degradation, defined by the damage parameter ω .

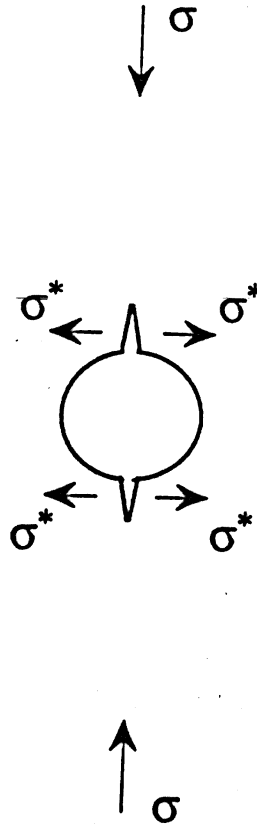


Figure 4.2. Local tensile stress σ^* (which drives the microcrack growth) arises in the vicinity of the pore.

5.0 SUMMARY AND CONCLUSIONS

The objective of this report was to summarize on-going research directed towards the formulation of a rational continuum model of a porous rock containing a large number of microcracks. The ultimate goal is to provide a versatile physically-based model suitable for large-scale, finite element-type computations. There is a considerable body of evidence that a variety of important features of rock deformation (such as dilatancy, compaction, brittle-ductile transition, etc.) cannot be modeled without consideration of the rock fabric and its influence on micromechanical processes. On the other hand, purely micromechanical models are computationally inefficient and, therefore, not suitable for such purposes.

In view of the program objective, the only rational solution is to develop a micromechanically-inspired constitutive model. The proposed model will retain the form and framework of conventional phenomenological theories. The details of the model, however, such as the selection of mathematical representations of the damage parameters, forms of evolution laws, etc., will be constructed in concert with micromechanical considerations of micromechanisms observed experimentally in real porous rocks (sandstones and limestones). Consequently, the material parameters of the model will be experimentally identifiable. However, their numerical values will require some minimal amount of curve fitting. An illustration of micromechanical modeling was presented in Sections 2.2 and 2.3.

The present study is at the stage where it focuses on brittle response by examining the geometry of microcracks and their influence on the response. Sections 3.1 and 3.2 concentrated on the physical description of damage defined by frictional crack surfaces in planes of various orientations passing through a material point. Various approximations of a typical damage distribution in porous rocks were illustrated in Sections 3.1 and 3.2. It is unlikely in real applications that a detailed crack density distribution will ever be available. Thus, it was argued that the second-order tensor damage parameter approximates the expected crack density distribution with sufficient accuracy in the case of proportional loading. The case of non-proportional loading is scheduled to be addressed in the sequel to this study.

Rigorous, novel, and elegant derivation of the effective (overall or equivalent) stiffness and compliance tensors was presented in Sections 3.3 and 3.4. The formulas for the exact inversions of these tensors were derived to enhance intended computational efficiency. Particular cases of isotropic and transversely isotropic damage distributions were derived not only as an illustration but more importantly as a guide to the determination of material parameters and the damage evolution law. Applications to the case of uniaxial and biaxial stress (compressive and/or tensile) loadings were illustrated in Section 3.5.

Section 4.0 provided additional guidelines in relating the proposed model to the physics of the process on the microscale. The emphasis was again on the enhancement of tensor manipulations of the stiffnesses and compliances. At each step the model constants were related to measurable

material parameters (see expressions (4.45), for example). The example in Section 4.5 provided an illustration of how the proposed model can be used in estimating accumulated damage during a given loading program. In addition to acoustic emission tests, this will provide a valuable means for determining damage evolution laws and/or the kinematics of the "damage surface".

In summary, the present model provides a general framework for a rational, micromechanically-inspired, continuum model for a porous rock. The model provides a novel viewpoint of the entire class of damage models. For the first time, clear arguments have been provided to facilitate the selection of the simplest (yet sufficiently accurate) representation of damage. Microcrack distributions, damage measures (parameters), and material parameters are firmly related to each other allowing for unambiguous experimental identifications of the quantities needed for modeling.

At this point the analysis is limited to purely brittle deformation processes and proportional loadings. Incorporation of ductile effects and the transition to rate models (necessary for non-proportional loadings) will be addressed in the sequel to this study and when requisite experimental data become available. In order to define the damage evolution law(s) and, perhaps, define a "damage surface", it will be necessary to carefully design an experimental program combining measurements of elastic moduli in three orthogonal directions along with acoustic emissions measurements. These experiments will have to be performed at several confining pressure levels for different loading programs in order to develop a reliable basis for the determination of the evolution law(s). A major problem, of course, is our inability to measure the microcrack density at each point directly. Thus, it becomes necessary to relate the microcrack distribution to macrostiffnesses, as was done in this report, and infer the former from the latter. The importance of this task is not evident from the problems considered in this report. However, in the case of non-proportional loading it will be necessary to know the orientation of cracks in order to estimate the discontinuous changes in elastic moduli associated with the changes in the signs of the normal stresses.

A few simple examples were used to illustrate the remarkable versatility and efficiency of the model in replicating the salient trends of the considered phenomena. Even in its present state of development the proposed model allows for a simple identification of the material parameters and their experimental measurement. In particular, it appears possible to determine the approximate distribution of damage densities by measuring the components of the stiffness tensor. The indenter test proposed by Zarka and Frelat (1977) could be particularly appropriate for this task.

The most important conclusion derived from the work reported herein is that it is indeed possible to complete this task and formulate a constitutive theory for rocks which will satisfy all requirements of efficiency and accuracy. The general form of this theory has already been put together in this report. However, a significant effort must still be mounted in order to achieve the ambitious goal of this overall research project.

6.0 REFERENCES

- Ashby, M.F., and Hallam, S.D. 1986 The failure of brittle solids containing small cracks under compressive stress states. *Acta Metall.* 34, 497-510.
- Bazant, Z.P., Tabbara, M.R., and Kazemi, M.T. 1989 Stable path of interacting crack systems and micromechanics of damage. In *Advances in fracture research, Proc. 7th Int. Conf. on Fracture (ICF7)*, Vol. 3, Houston, TX, pp. 2141-2152.
- Bazant, Z.P., and Cedolin, L. 1991 *Stability of structures*. Oxford University Press, New York, NY.
- Byerlee, J.D., and Brace, W.F. 1969 High pressure mechanical instability in rocks. *Science* 164, 713-715.
- Budiansky, B., and O'Connell, R.J. 1976 Elastic moduli of a cracked solid. *Int. J. Solids Structures* 12, 81-97.
- Budiansky, B., and Rice, J.R. 1973 Conservation laws and energy-release rates. *J. Appl. Mech.* 40, 201-203.
- Chaboche, J.L. 1992 Damage induced anisotropy: On the difficulties associated with the active/passive unilateral condition. *Int. J. of Damage Mechanics* 1, 148-171.
- Chow, C.L., and Wang, J. 1988 Ductile fracture characterization with an anisotropic continuum damage theory. *Engng. Frac. Mech.* 30, 547-563.
- Conrad, R.E., and Friedman, M. 1976 Microscopic feather fractures in the faulting process. *Tectonophysics* 33, 187-198.
- Costin, L.S. 1985 Damage mechanics in the post-failure regime. *Mechanics of Materials* 4, 149-160.
- Dragon, A., and Mroz, Z. 1979 A continuum model for plastic brittle behavior of rock and concrete. *Int. J. Eng. Sci.* 17, 121-137.
- Dundurs, J., and Markenscoff, X. 1989 A Green's function formulation of anticracks and their interaction with load-induced singularities. *J. Appl. Mech.* 56, 550-555.
- Englman, R., Murat, M. and Jaeger, Z. 1992 Crack cluster description of fracture: Thermodynamical energy functionals and numerical study. *Phys. Rev. B* 45, 10331-10337.
- Evans, B., Fredrich, J.T., and Wong, T.-f. 1990 The brittle-ductile transition in rocks: Recent experimental and theoretical progress. In *The brittle-ductile transition in rocks. The Heard Volume, Geophys. Monogr. Ser.*, Vol. 56 (ed. A.G. Duba, et al.), AGU, Washington, D.C., pp. 1-20.

- Felice, C.W., Norman, D., and Senseny, P.E. 1991 A physical assessment of test specimens in the post-peak regime. In *Rock mechanics as a multidisciplinary science*, (ed. J.C. Roegiers) Balkema, Rotterdam, pp. 283-292.
- Hallbauer, D.K., Wagner, H., and Cook, N.G.W. 1973 Some observations concerning the microscopic and mechanical behavior of quartzite specimens in stiff, triaxial compression tests. *Int. J. Rock Mech. Sci & Geomech. Abstr.* 10, 713-726.
- Hasebe, N., and Ueda, M. 1980 Crack originating from a corner of a square hole. *Engg. Frac. Mechs.* 13, 913-923.
- Hill, R. 1967 The essential structure of constitutive laws for metal composites and polycrystals. *J. Mech. Phys. Solids* 15, 79-95.
- Hirth, G., and Tullis, J. 1989 The effects of pressure and porosity on the micromechanics of the brittle-ductile transition in quartzite. *J. Geophys. Res.* 94, 17,825-17,838.
- Holcomb, D.J., and Costin, L.S. 1986 Detecting damage surfaces in brittle materials using acoustic emissions. *J. Appl. Mech.* 53, 536-544.
- Holcomb, D.J., Stone, C.M., and Costin, L.S. 1990 Combining acoustic emission locations and a microcrack damage model to study development of damage in brittle materials. In *Rock mechanics contributions and challenges* (ed. Hustrulid & Johnson), Balkema, Rotterdam, pp. 645-651.
- Horii, H., and Nemat-Nasser, S. 1983 Overall moduli of solids with microcracks: Load-induced anisotropy. *J. Mech. Phys. Solids* 31, 155-171.
- Horii, H., and Nemat-Nasser, S. 1986 Brittle failure in compression: splitting, faulting and brittle-ductile transition. *Phil. Trans. R. Soc. Lond. A* 319, 337-374.
- Hustrulid, W., and Robinson, F. 1973 A simple stiff machine for testing rock in compression. In *New horizons in rock mechanics* (ed. H.R. Hardy & R. Stefanko), 14th Symp. Rock Mechs., ASCE, New York, pp. 61-84.
- Isida, M., and Nemat-Nasser, S. 1987 On mechanics of crack growth and its effects on the overall response of brittle porous solids. *Acta Metall.* 35, 2887-2898.
- Jaeger, J.C., and Cook, N.G.W. 1976 *Fundamentals of rock mechanics*. Chapman and Hall, London.
- Jones, L.M. 1980 Cyclic loading of simulated fault gouge to large strains. *J. Geophys. Res.* 85, 1826-1832.
- Ju, J.W. 1989 On energy-based coupled elastoplastic damage theories: Constitutive modeling and computational aspects. *Int. J. Solids Structures* 25, 803-833.
- Kachanov, L.M. 1958 On the creep rupture time. *Izv. AN SSSR, Otd. Tekhn. Nauk* 8, 26-31.

- Kachanov, M. 1980 Continuum model of medium with cracks. *J. Engng. Mech. Div. ASCE* 106, 1039-1051.
- Kachanov, M. 1982 A microcrack model of rock inelasticity- Part I: Frictional sliding on micro-cracks. *Mechanics of Materials* 1, 19-27.
- Kachanov, M. 1992 Effective elastic properties of cracked solids: Critical review of some basic concepts. In *Micromechanical modeling of quasi-brittle materials behavior* (ed. V.C. Li), ASME Book No. AMR118, pp. 304-335.
- Kanatani, K. 1984 Distribution of directional data and fabric tensors. *Int. J. Engng. Sci.* 22, 149-164.
- Kanninen, M.F., and Popelar, C.H. 1985 *Advanced fracture mechanics*, Oxford University Press, New York, NY.
- Kemeny, J.M., and Cook, N.G.W. 1991 Micromechanics of deformation in rocks. In *Toughening mechanisms in quasi-brittle materials* (ed. S.P. Shah), Kluwer Acad. Publish, pp. 155-188.
- Kouris, D., and Tsuchida, E. 1991 On the elastic interaction between two fibers in a continuous fiber composite under thermal loading. *Mechanics of Materials* 12, 131-146.
- Krajcinovic, D. 1989 Damage mechanics. *Mechanics of Materials* 8, 117-197.
- Krajcinovic, D., and Fanella, D. 1986 A micromechanical damage model for concrete. *Eng. Fract. Mech.* 25, 585-596.
- Krajcinovic, D., and Fonseka, G.U. 1981 The continuous damage theory of brittle materials. Part 1: General theory. *J. Appl. Mech.* 48, 809-815.
- Kranz, R.L. 1983 Microcracks in rocks: A review. *Tectonophysics* 100, 449-480.
- Kunin, I.A. 1983 *Elastic media with microstructure II*. Springer Verlag, Berlin.
- Lekhnitskii, S.G. 1981 *Theory of elasticity of an anisotropic body*. Mir Publishers, Moscow.
- Lemaitre, J. 1987 Formulation and identification of damage kinetic constitutive equations. In *Continuum damage mechanics- Theory and application* (ed. D. Krajcinovic & J. Lemaitre), CISM Courses and Lectures No. 295, Springer Verlag, Wien, pp. 37-89.
- Lemaitre, J. 1992 *A course on damage mechanics*. Springer Verlag, Berlin.
- Lockner, D.A., and Byerlee, J.D. 1991 Precursory AE patterns leading to rock fracture. In *Proc. 5th Conf. on acoustic emission/Microseismic activity in geologic structures and materials* (ed. H.R. Hardy), Trans-tech. Publ., Clausthal-Zellerfeld, Germany.

- Lockner, D.A., Byerlee, J.D., Kuksenko, V., Ponomarev, A., and Sidorin, A. 1992 Observations of quasistatic fault growth. In *Fault mechanisms and transport properties of rocks*, (ed. B. Evans, and T.-f. Wong), Academic Press, London, pp. 3-32.
- Murakami, S. 1988 Mechanical modeling of material damage. *J. Appl. Mech.* 55, 280-286.
- Nemat-Nasser, S., and Shokooh, A. 1980 On finite plastic flows of compressible materials with internal friction. *Int. J. Solids Structures* 16, 495-514.
- Nemat-Nasser, S., and Obata, M. 1988 A microcrack model of dilatancy in brittle materials. *J. Appl. Mech.* 55, 24-35.
- Nemat-Nasser, S., and Hori, M. 1990 Elastic solids with microdefects. In *Micromechanics and inhomogeneity- The Toshio Mura anniversary volume* (ed. G.J. Weng, M. Taya & H. Abé), Springer Verlag, New York, pp. 297-320.
- Olsson, W.A. 1974 Microfracturing and faulting in a limestone. *Tectonophysics* 24, 277-285.
- Onat, E.T., and Leckie, F.A. 1988 Representation of mechanical behavior in the presence of changing internal structure. *J. Appl. Mech.* 55, 1-10.
- Ortiz, M. 1985 A constitutive theory for the inelastic behavior of concrete. *Mechanics of Materials* 4, 67-93.
- Paterson, M.S. 1978 *Experimental rock deformation - The brittle field*. Springer Verlag, New York.
- Rice, J.R. 1975 Continuum mechanics and thermodynamics of plasticity in relation to microscale deformation mechanisms. In *Constitutive equations in plasticity* (ed. A.S. Argon), MIT Press, Cambridge, MA, pp. 23-79.
- Rooke, D.P., and Cartwright, D.J. 1976 *Compendium of stress intensity factors*, H.M.S.O., England.
- Rudnicki, J.W., and Rice, J.R. 1975 Conditions for the localization of deformation in pressure-sensitive dilatant materials. *J. Mech. Phys. Solids* 23, 371-394.
- Rutter, E.H., and Hadizadeh, J. 1991 On the influence of porosity on the low-temperature brittle-ductile transition in siliciclastic rocks. *J. Struct. Geol.* 13, 609-614.
- Sammis, C.G., and Ashby, M.F. 1986 The failure of brittle porous solids under compressive stress states. *Acta. Metall.* 34, 511-526.
- Sangha, C.M., Talbot, C.J., and Dhir, R.K. 1974 Microfracturing of a sandstone in uniaxial compression. *Int. J. Rock Mech. & Min. Sci.* 11, 107-113.
- Savin, G.N. 1961 *Stress concentration around holes*, Pergamon Press, New York.

- Simo, J.C., and Ju, J.W. 1987 Strain- and stress-based continuum damage models- I. Formulation. *Int. J. Solids Structures* 23, 821-840.
- Spencer, A.J.M. 1971 Theory of invariants. In *Continuum physics* (ed. A.C. Eringen), vol. 1, Academic Press, New York, pp. 239-253.
- Sumarac, D. 1987 Self-consistent model for the brittle response of solids. *PhD Thesis*, University of Illinois at Chicago.
- Swolfs, H.S. 1972 Chemical effects of pore fluids on rock properties. *Am. Assoc. Petrol. Geol. Mem.* 18, 224-233.
- Tada, H., Paris, P.C., and Irwin, G.R. 1985 *The stress analysis of cracks handbook*. Del Research Corporation, St. Louis, Mo.
- Talreja, R. 1985 A continuum mechanics characterization of damage in composite materials. *Proc. R. Soc. London A* 399, 195-216.
- Underwood, E.E. 1970 *Quantitative stereology*, Addison Wesley, Reading, MA.
- Vakulenko, A.A., and Kachanov, M.L. 1971 Continuum theory of cracked media. *Mekhanika Tverdogo Tela* 4, 159-166 (in Russian).
- Wong, T.-f. 1985 Geometric probability approach to the characterization and analysis of microcracking in rocks. *Mech. of Mater.* 4, 261-276.
- Wong, T.-f. 1990 Mechanical compaction and the brittle-ductile transition in porous sandstones. In *Deformation mechanisms, rheology and tectonics* (ed. R.J. Knipe & E.H. Rutter), Geological Society Special Publication no 54, pp. 111-122.
- Wong, T.-f., and Biegel, R. 1985 Effects of pressure on the micromechanics of faulting in San Marcos gabbro. *J. Struct. Geol.* 7, 737-749.
- Wong, T.-f., Szeto, H., and Zhang, J. 1992 Effect of loading path and porosity on the failure mode of porous rocks. *Appl. Mech. Rev.* 45, 281-293.
- Zarka, J., and Frelat, J. 1977 On a description of a new "hardness" test. *Int. J. Solids Structures* 13, 493-502.
- Zhang, J., Wong, T.-f., and Davis, D.M. 1989 The brittle to ductile transition in porous sandstones. *EOS, Trans. Amer. Geophys. Union* 70, 1360-1368.
- Zhang, J., Wong, T.-f., and Davis, D.M. 1990a Micromechanics of pressure-induced grain crushing in porous rocks. *J. Geophys. Res.* 95, 341-352.
- Zhang, J., Wong, T.-f., Yanagidani, T., and Davis, D.M. 1990b Pressure-induced microcracking and grain crushing in Berea and Boise sandstones: Acoustic emission and quantitative microscopy measurements. *Mech. Mater.* 9, 1-15.

- Zheng, Z. 1989 Compressive stress-induced microcracks in rocks and applications to seismic anisotropy and borehole stability. *PhD thesis*, University of California, Berkeley.
- Zheng, Z., McLennan, J., and Martin, W. 1991 Compressive stress-induced microcracks and effective elastic properties of limestone and concrete. *Phase I final technical report*, submitted to AFOSR/XOT by Terra Tek, Inc.

DISTRIBUTION LIST

DEPARTMENT OF DEFENSE

Director
Defense Nuclear Agency
ATTN: DFSP (Mr. C. B. McFarland)
SPSP (Mr. A. A. Frederickson)
SPWE (Dr. L. A. Wittwer)
SPWE (Dr. E. L. Tremba)
SPSD (Dr. P. E. Senseny)
SPSD (Mr. M. E. Giltrud)
Technical Library
6801 Telegraph Road
Alexandria, VA 22310-3398

Commander
Field Command, Defense Nuclear Agency
ATTN: FCT-S (Dr. G. Y. Baladi)
FCTT (Dr. Byron Ristvet)
FCTTSP (Dr. E. J. Rinehart)
FCTTS (Dr. P. W. Randles)
1680 Texas St., SE
Kirtland AFB, NM 87117-5669

Director
Advanced Research Project Agency
ATTN: Library
3701 N. Fairfax Drive
Arlington, VA 22203-1714

Director
Defense Intelligence Agency
ATTN: Unclassified Library
Washington, DC 20340

Defense Technical Information Center
ATTN: TC (2 cys)
Cameron Station
Alexandria, VA 22314

DEPARTMENT OF THE ARMY

Commander
US Army Corps of Engineers
ATTN: CERD-ZA (Dr. R. B. Oswald)
CERD-L (Mr. D. C. May)
CERD-M (Dr. D. J. Leverenz)
CERD-M (Mr. J. R. Lundien)
CEMP-ET (Mr. Al Knoch)
CEIM-SL (2 cys)
Washington, DC 20314-1000

DEPARTMENT OF THE ARMY (CONTINUED)

Commander & Director
US Army Construction Engineering Research
Laboratory
ATTN: Technical Library
P.O. Box 9005
Champaign, IL 61826-9005

Commander
US Army Engineer District, Omaha
ATTN: CEMRO-ED-SH (Mr. W. H. Gaube)
215 North 17th Street
Omaha, NE 68102-4978

Director
US Army Cold Regions Research and
Engineering Laboratory
ATTN: Technical Library
72 Lyme Road
Hanover, NH 03755-1290

Commander
US Army Research Laboratory
ATTN: Technical Library
2800 Powder Mill Road
Adelphi, MD 20783-1145

Director
US Army Research Laboratory
ATTN: Technical Library
Aberdeen Proving Ground, MD 21005-5066

Director
US Army Research Office
ATTN: SLCRO-IP-L (Ms. Brenda Mann)
P.O. Box 12211
Research Triangle Park, NC 27709-2211

Commander
US Army Nuclear and Chemical Agency
ATTN: Technical Library
7500 Backlick Road, Bldg. 2073
Springfield, VA 22150

DEPARTMENT OF THE NAVY

Naval Facilities Engineering Service Center
ATTN: Technical Library
Code L51 (Mr. R. J. Odello)
560 Center Drive
Port Hueneme, CA 93043-4328

Naval Facilities Engineering Command
200 Stovall Street
ATTN: Technical Library
Alexandria, VA 22332-2300

DEPARTMENT OF THE AIR FORCE

Air Force Institute of Technology
Air University
ATTN: Technical Library
Wright-Patterson AFB, OH 45433

Air Force Office of Scientific Research
ATTN: NA (Maj M. D. Lewis)
Technical Library
Bolling AFB, DC 20332

Phillips Laboratory
ATTN: Technical Library
Kirtland AFB, NM 87117-6008

Wright Laboratory
Airbase Survivability Branch
ATTN: WL/FIVCS-OL (Mr. W. S. Strickland)
Technical Library
139 Barnes Drive, Suite 2
Tyndall AFB, FL 32403-5323

Commander
Wright Laboratory
Armament Directorate
ATTN: MNMW (Dr. W. H. Cook)
Technical Library
101 W. Eglin Blvd., Ste 251
Eglin AFB, FL 32542-6810

DEPARTMENT OF ENERGY

Lawrence Livermore National Laboratory
ATTN: L-53 (Technical Library)
P.O. Box 808
Livermore, CA 94550-0622

DEPARTMENT OF ENERGY (CONTINUED)

Los Alamos National Laboratory
ATTN: M/S F665 (Charles Snell, EES-5)
M/S P364 (Report Library)
P.O. Box 1663
Los Alamos, NM 87545

Sandia National Laboratories
ATTN: Dept 1433 (D. E. Grady)
Dept 9723 (Dr. Vincent Luk)
Dept 7141 (Technical Library)
P.O. Box 5800
Albuquerque, NM 87185-5800

DEPARTMENT OF THE INTERIOR

U.S. Geological Survey
ATTN: Dr. David A. Lockner/MS 977
345 Middlefield Road
Menlo Park, CA 94025

U.S. Geological Survey
ATTN: MS-928 (Dr. Bill Leith)
12201 Sun Rise Valley Drive
Reston, VA 22092

DEPARTMENT OF DEFENSE CONTRACTORS

Mr. J. L. Bratton
Mr. D. M. Cole
Applied Research Associates, Inc.
4300 San Mateo Blvd., NE, Suite A220
Albuquerque, NM 87110

Mr. S. E. Blouin
Applied Research Associates, Inc.
Box 120A, Waterman Road
South Royalton, VT 05068

Mr. R. E. Walker
Applied Research Associates, Inc.
3202 Wisconsin Avenue
Vicksburg, MS 39180

Dr. J. G. Trulio
Applied Theory, Inc.
3355 Spring Mountain Road, Suite 57
Las Vegas, NV 89102

DEPARTMENT OF DEFENSE CONTRACTORS (CONT.)

Dr. Dusan Krajcinovic (4 cys)
Dr. Vlado Lubarda (4 cys)
Mechanical and Aerospace Engineering
Arizona State University
Tempe, AZ 85287-6106

Dr. T. J. Ahrens
California Institute of Technology
Seismological Laboratory/252-21
Pasadena, CA 91125

Dr. Hon-Yim Ko
Department of Civil, Environmental, and
Architectural Engineering
University of Colorado at Boulder
Boulder, CO 80309

Dr. Martin Ostojka-Starzewski
Department of Metallurgy, Mechanics and
Materials Science
Michigan State University
East Lansing, MI 48824-1226

Dr. Zdenek P. Bazant
Department of Civil Engineering
Northwestern University
Evanston, IL 60208-3109

Dr. J. W. Ju
Department of Civil Engineering and
Operations Research
Princeton University
Princeton, NJ 08544

Dr. Dwayne Piepenburg
Logicon RDA
6940 S. Kings Hwy, Suite 210
Alexandria, VA 22310

Dr. Howdy Pratt
Science Applications International
Corporation
10260 Campus Point Dr.
San Diego, CA 92121

Dr. D. F. Patch
Science Applications International
Corporation
10260 Campus Pt. Dr., M/S C2
San Diego, CA 92121

DEPARTMENT OF DEFENSE CONTRACTORS (CONT.)

Dr. Ed Peterson
Dr. K. D. Pyatt, Jr.
S-CUBED
A Division of Maxwell Labs, Inc.
P.O. Box 1620
La Jolla, CA 92038-1620

Springfield Research Facility
ATTN: Dr. Dwayne Kicker
P.O. Box 1220
5400 Port Royal Road
Springfield, VA 22151

Dr. A. L. Florence
Dr. Lynn Seaman
Technical Library
SRI International
333 Ravenswood Avenue
Menlo Park, CA 94025

Dr. A. H. Jones
Terra Tek, Inc.
420 Wakara Way
Salt Lake City, UT 84108

Dr. Y. Marvin Ito
Titan Research & Technology
9410 Topanga Canyon Blvd., Suite 104
Chatsworth, CA 91311-5771

Mr. Norman Lipner
TRW Defense Systems Group
P.O. Box 1310
San Bernardino, CA 92402

Dr. I. S. Sandler
Weidlinger Associates
333 Seventh Avenue
New York, NY 10001

Dr. Jeremy Isenberg
Weidlinger Associates
4410 El Camino Real, Suite 110
Los Altos, CA 94022

REPORT DOCUMENTATION PAGEForm Approved
OMB No. 0704-0188

Public reporting burden for this collection of information is estimated to average 1 hour per response, including the time for reviewing instructions, searching existing data sources, gathering and maintaining the data needed, and completing and reviewing the collection of information. Send comments regarding this burden estimate or any other aspect of this collection of information, including suggestions for reducing this burden, to Washington Headquarters Services, Directorate for Information Operations and Reports, 1215 Jefferson Davis Highway, Suite 1204, Arlington, VA 22202-4302, and to the Office of Management and Budget, Paperwork Reduction Project (0704-0188), Washington, DC 20503.

| | | | | |
|---|---|--|---|-----------------------------------|
| 1. AGENCY USE ONLY (Leave blank) | | 2. REPORT DATE February 1994 | 3. REPORT TYPE AND DATES COVERED Final report | |
| 4. TITLE AND SUBTITLE Constitutive Modeling of Rocks with Internal Cracks and Pores | | | 5. FUNDING NUMBERS FY92 WU Code 00002 (Task 4) Contract No. DACA39-92-M-1980 | |
| 6. AUTHOR(S) D. Krajcinovic, V. Lubarda | | | | |
| 7. PERFORMING ORGANIZATION NAME(S) AND ADDRESS(ES) Arizona State University Tempe, AZ 85287-6106 | | | 8. PERFORMING ORGANIZATION REPORT NUMBER | |
| 9. SPONSORING/MONITORING AGENCY NAME(S) AND ADDRESS(ES) Defense Nuclear Agency 6801 Telegraph Road, Alexandria, VA 22310-3398; U.S. Army Engineer Waterways Experiment Station Structures Laboratory 3909 Halls Ferry Road, Vicksburg, MS 39180-6199 | | | 10. SPONSORING/MONITORING AGENCY REPORT NUMBER Contract Report SL-94-1 | |
| 11. SUPPLEMENTARY NOTES Available from National Technical Information Service, 5285 Port Royal Road, Springfield, VA 22161. | | | | |
| 12a. DISTRIBUTION / AVAILABILITY STATEMENT Approved for public release; distribution is unlimited. | | | 12b. DISTRIBUTION CODE | |
| 13. ABSTRACT (Maximum 200 words) The report considers fundamental issues of the constitutive modeling of rocks with internal cracks and pores. Phenomenological and micromechanically inspired damage models for brittle deformation of rocks are formulated. Representation of damage by various order damage tensors and derivation of the corresponding effective elastic stiffness and compliance tensors are given. Isotropic and transversely isotropic responses are considered, with applications to uniaxial and biaxial stress loadings. The presented model provides a general framework for a rational, micromechanically inspired, continuum modeling of brittle porous rocks. | | | | |
| 14. SUBJECT TERMS Brittle response Pores Limestone Rock Microcracks Stress-strain | | | 15. NUMBER OF PAGES 70 | |
| | | | 16. PRICE CODE | |
| 17. SECURITY CLASSIFICATION OF REPORT UNCLASSIFIED | 18. SECURITY CLASSIFICATION OF THIS PAGE UNCLASSIFIED | 19. SECURITY CLASSIFICATION OF ABSTRACT | | 20. LIMITATION OF ABSTRACT |